IFRD1 is required for maintenance of bladder epithelial homeostasis

Graphical abstract

Highlights

- IFRD1 plays a key role in maintaining urothelial homeostasis in the bladder

- Loss of IFRD1 leads to dysregulated urothelial homeostasis

- Loss of IFRD1 triggers ER stress, PERK pathway activation, and oxidative stress

- IFRD1 loss impairs urothelial barrier function and leads to aberrant voiding behavior

Authors

Bisiayo E. Fashemi, Amala K. Rougeau, Arnold M. Salazar, ..., Charles J. Cho, Jason C. Mills, Indira U. Mysorekar

Correspondence

jason.mills@bcm.edu (J.C.M.),
indira.mysorekar@bcm.edu (I.U.M.)

In brief

Physiology; Cell biology; Transcriptomics

CellPress

iScience

Article

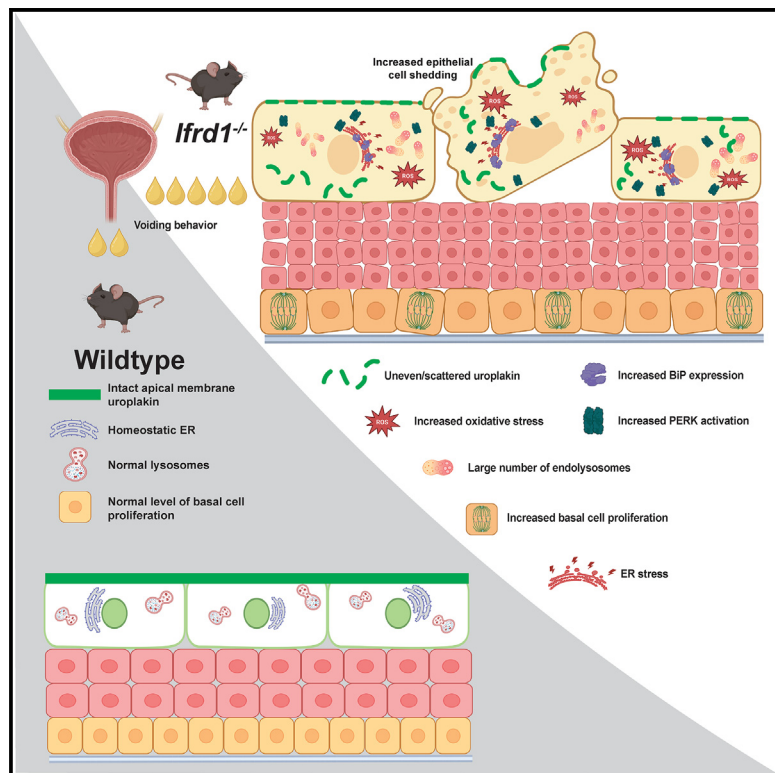# IFRD1 is required for maintenance of bladder epithelial homeostasis

Bisiayo E. Fashemi,[1,9] Amala K. Rougeau,[2,9] Arnold M. Salazar,[3,9] Steven J. Bark,[2,3] Rayvanth Chappidi,[1] Jeffrey W. Brown,[4] Charles J. Cho,[2] Jason C. Mills,[2,5,6,*] and Indira U. Mysorekar[3,7,8,10,*]

[1]Department of Obstetrics and Gynecology, Center for Reproductive Health Sciences, Washington University School of Medicine, St. Louis, MO 63110, USA
[2]Department of Medicine, Section of Gastroenterology and Hepatology, Baylor College of Medicine, 1 Baylor Plaza, Houston, TX 77030, USA
[3]Department of Medicine, Section of Infectious Diseases, Baylor College of Medicine, 1 Baylor Plaza, Houston, TX 77030, USA
[4]Department of Medicine, Division of Gastroenterology, Washington University School of Medicine, St. Louis, MO 63110, USA
[5]Department of Pathology and Immunology, Baylor College of Medicine, 1 Baylor Plaza, Houston, TX 77030, USA
[6]Department of Molecular and Cellular Biology, Baylor College of Medicine, 1 Baylor Plaza, Houston, TX 77030, USA
[7]Department of Molecular Virology and Microbiology, Baylor College of Medicine, 1 Baylor Plaza, Houston, TX 77030, USA
[8]Huffington Center on Aging, Baylor College of Medicine, 1 Baylor Plaza, Houston, TX 77030, USA
[9]These authors contributed equally
[10]Lead contact
*Correspondence: jason.mills@bcm.edu (J.C.M.), indira.mysorekar@bcm.edu (I.U.M.)
https://doi.org/10.1016/j.isci.2024.111282

SUMMARY

The maintenance of homeostasis and rapid regeneration of the urothelium following stress are critical for bladder function. Here, we identify a key role for IFRD1 in maintaining urothelial homeostasis in a mouse model. We demonstrate that the murine bladder expresses IFRD1 at homeostasis, particularly in the urothelium, and its loss alters the global transcriptome with significant accumulation of endolysosomes and dysregulated uroplakin expression pattern. We show that IFRD1 interacts with mRNA-translation-regulating factors in human urothelial cells. Loss of *Ifrd1* leads to disrupted proteostasis, enhanced endoplasmic reticulum (ER stress) with activation of the PERK arm of the unfolded protein response pathway, and increased oxidative stress. *Ifrd1*-deficient bladders exhibit urothelial cell apoptosis/exfoliation, enhanced basal cell proliferation, reduced differentiation into superficial cells, increased urothelial permeability, and aberrant voiding behavior. These findings highlight a crucial role for IFRD1 in urothelial homeostasis, suggesting its potential as a therapeutic target for bladder dysfunction.

INTRODUCTION

The urinary bladder has the primary function of storing and releasing urine. At its center, the lumen is lined with a pseudo-stratified transitional layer called urothelium, which comprises three main cell types, namely superficial, intermediate, and basal urothelial cells. The superficial cells harbor four uroplakin proteins (Ia, Ib, II, and III) that localize and assemble on the apical plasma membrane, forming a highly specialized impermeable barrier that protects the mucosa from toxic factors in urine.[1] Under homeostatic conditions, the urothelium is quiescent and has the slowest turnover of any mammalian epithelium.[2–4] However, upon injury, a rapid activation of regenerative response in the basal (cytokeratin 5+ cells) leading to complete restoration of the superficial cell layer within 72 h post injury is observed.[5–10] A number of factors have been identified to play important roles in urothelial development, injury, and disease response.[11–14]

The bladder undergoes distension-contraction cycles as it fills and voids throughout each day and across the whole lifespan. During distension, structural changes in the urothelium rely on the intracellular discoidal fusiform vesicles lined with uroplakins in the superficial cells that undergo coordinated exocytosis with apical membrane endocytosis.[15–19] The uroplakin proteins are then recycled via endocytosis and multivesicular bodies (MVBs) trafficking to decrease the size of the urothelial membrane upon contraction.[20–23] Also, endocytosed membrane and damaged uroplakins can be routed from MVBs to lysosomes for degradation.[19–23] This cycle happens regularly and clearly demonstrates the continual exposure of the bladder to tensile forces of stretching and contraction. Further, any aberrations in the cycle that promote damage in the tissue and eventual infiltration of toxic wastes and molecules into the urothelium can add more burden and stress. However, the molecular mechanisms underpinning how the urothelium maintains homeostasis under this state of constant stress are not well understood.

The interferon-related developmental regulator 1 (IFRD1, a.k.a PC4 and TIS7) encodes a protein involved in various cellular processes, including cell growth, differentiation, and response to stress.[24–26] IFRD1 was initially identified as an immediate-early gene that was transiently and rapidly induced by nerve growth

factor in a pheochromocytoma (PC) cell line and by phorbol esters (IFRD1, a.k.a PC4 and TIS7).[27] In general, it has been shown to be an injury-inducible gene stimulated by a multitude of agents and conditions such as tunicamycin,[28,29] sodium arsenite, and amino acid starvation,[30] with such injuries increasing IFRD1 in human kidney and cervical cancer cells and mouse embryonic fibroblast cells. Furthermore, partial hepatectomy of the liver,[31] cerulein treatment in pancreas,[32] high-dose tamoxifen treatment in the stomach,[32] tunicamycin treatment in kidney,[30] and resection in the small bowel[33] increase IFRD1 expression. Thus, IFRD1 expression is a cellular stress response.[28,29] In the absence of injury, otherwise healthy, young adult *Ifrd1*^{−/−} mice have largely been reported *not* to have homeostatic phenotypes in diverse organs[30,34,35] to date. However, a role for IFRD1 has also not been explored in the bladder mucosa.

In this study, we show the expression of IFRD1 in the urinary bladder even at homeostasis and that loss of IFRD1 promotes significant molecular, cellular, and organellar alterations in the urothelium. Cytological and immunological assays demonstrate that loss of IFRD1 significantly increases endolysosomes and promotes abnormal distribution of uroplakins in the urothelium. Transcriptomic analysis reveals that loss of IFRD1 significantly impacts global translation levels in the bladder characterized by substantial alterations in the expression of genes involved in the functional regulation of mitochondria, endoplasmic reticulum (ER), and the cell cycle. We further show that loss of IFRD1 increases ER stress, activates unfolded protein response (UPR), enhances reactive oxygen species (ROS) production, increases cell death markers, and increases epithelial cell shedding into the urine. Finally, we note that loss of IFRD1 reduces urothelial regenerative capacity, increases urothelial permeability, and promotes aberrant voiding behavior in mice. Overall, our study demonstrates the importance of IFRD1 in maintaining bladder homeostasis and suggests that maintenance of barrier function is an active process that requires translational machinery.

RESULTS

IFRD1 is expressed in the urothelium at homeostasis

Previous work from our group and others has shown that IFRD1 is expressed in multiple tissues at homeostasis in mice. However, studies of IFRD1 function in the bladder have not been reported. We extracted proteins from whole bladders of wild-type (WT) and *Ifrd1*^{−/−} mice, and western blotting revealed a robust expression of IFRD1in the former (Figure 1A, lane 1). As expected, no IFRD1 was detected in the *Ifrd1*^{−/−} bladders (Figure 1A, lane 2). To determine if IFRD1 was expressed in urothelial cells, we stripped the epithelium from the rest of the organ, and we again saw IFRD1 expression (Figure 1A, lane 3). We next examined the distribution/localization of IFRD1 in the urothelium using a genetic reporter system. We took advantage of a *lacZ* reporter that was cloned in-frame to exon 2 in the *Ifrd1* alleles in *Ifrd1*^{−/−} mice, which encodes for an IFRD1 (amino acids 1–43)-β-galactosidase fusion protein.[34] The system enables the visualization of *Ifrd1* expression by X-gal staining when one or both mutant *Ifrd1* alleles are present: namely, *Ifrd1*-expressing tissues/cells turn dark blue. Using fresh frozen bladder sections, X-gal staining (described in[36]) revealed expression in the super-

ficial urothelial cell layer of *Ifrd1*^{−/−} mice, whereas, as expected, no stain was observed in the WT mice (Figure 1B). Additionally, we performed the same assay on sections made from bladders that had first been fixed as a whole organ using the cross-linking fixative (containing glutaraldehyde) required for X-gal. Again, we noted strong blue stain in the urothelium (Figure 1C). In previous work, we have found IFRD1 mostly to be absent in homeostatic organs, though we do see some IFRD1 expression in acinar cells of pancreas at homeostasis. Accordingly, X-gal was positive in pancreas and negative in kidney, another organ of the urinary tract[30] (Figures 1D and 1E). To document the previously reported role of *Ifrd1* as largely an injury-induced gene, we injured the stomach with a high-dose tamoxifen model that we have previously characterized,[30,32,34,35] wherein high-dose tamoxifen induces IFRD1 expression in the murine stomach to help execute the conserved cellular regeneration program known as paligenosis.[32] As expected, only the digestive-enzyme-secreting chief cells in tamoxifen-injured *Ifrd1*^{−/−} mouse stomachs were positive (Figures 1F and 1G; insets highlight chief cells). Broadly, our findings corroborate the known pattern of *Ifrd1* expression, which is that it is largely absent at baseline in most organs but induced by injury. Note that injury that induces paligenosis further increases IFRD1 expression, and *Ifrd1*^{−/−} mice do not have a pancreatic, homeostatic phenotype.[32] Finally, our findings suggest that IFRD1 is expressed in the bladder at homeostasis, specifically in the urothelium.

Loss of IFRD1 causes alterations in urothelial cellular architecture and molecular pathways

To assess how the loss of IFRD1 affects the global environment of the bladder at homeostasis, we performed total RNA sequencing (RNAseq) on WT and *Ifrd1*^{−/−} mice. In comparison with WT, *Ifrd1*^{−/−} bladders displayed at least 1.5-fold (FDR-adjusted $p < 0.05$) decreased expression of 53 genes and increased expression of 161 genes (Figure 2A). Gene set enrichment analysis using MSigDB collections identified statistically significant upregulation of 8 pathways in WT versus *Ifrd1*^{−/−} mice and 20 pathways in *Ifrd1*^{−/−} versus WT mice (Figure 2B). Notably, these altered pathways included protein secretion, reactive oxygen species, oxidative phosphorylation, and fatty acid metabolism pathways (Figure 2B), all of which are critical for urothelial function. To determine whether these transcriptional alterations were correlated with histological changes associated with the bladder tissue, we performed H&E staining of the unperturbed WT and *Ifrd1*^{−/−} urothelium (Figure 2C). *Ifrd1*^{−/−} bladders were notable for harboring luminal cellular debris. Also, *Ifrd1*^{−/−} urothelial cells showed consistent and marked increase in intracellular vesicles (Figure 2C, bottom panel) and altered morphology (Figure S1). Transmission electron microscopy (TEM) revealed accumulation of MVBs (red arrow), as recognized by their characteristic, i.e., vesicle-within-vesicle morphology, in *Ifrd1*^{−/−} superficial cells (Figure 2C). Although the MVBs in WT superficial cells had lumens with the characteristic electron-lucent ("empty") or amorphous material (Figure 2D, image 1), the majority of MVBs of *Ifrd1*^{−/−} superficial cells were found to be fused with lysosomes, forming endolysosomes noted by their electron-dense material (Figure 2D, image 3, white arrows and inset). There was a significant difference in the
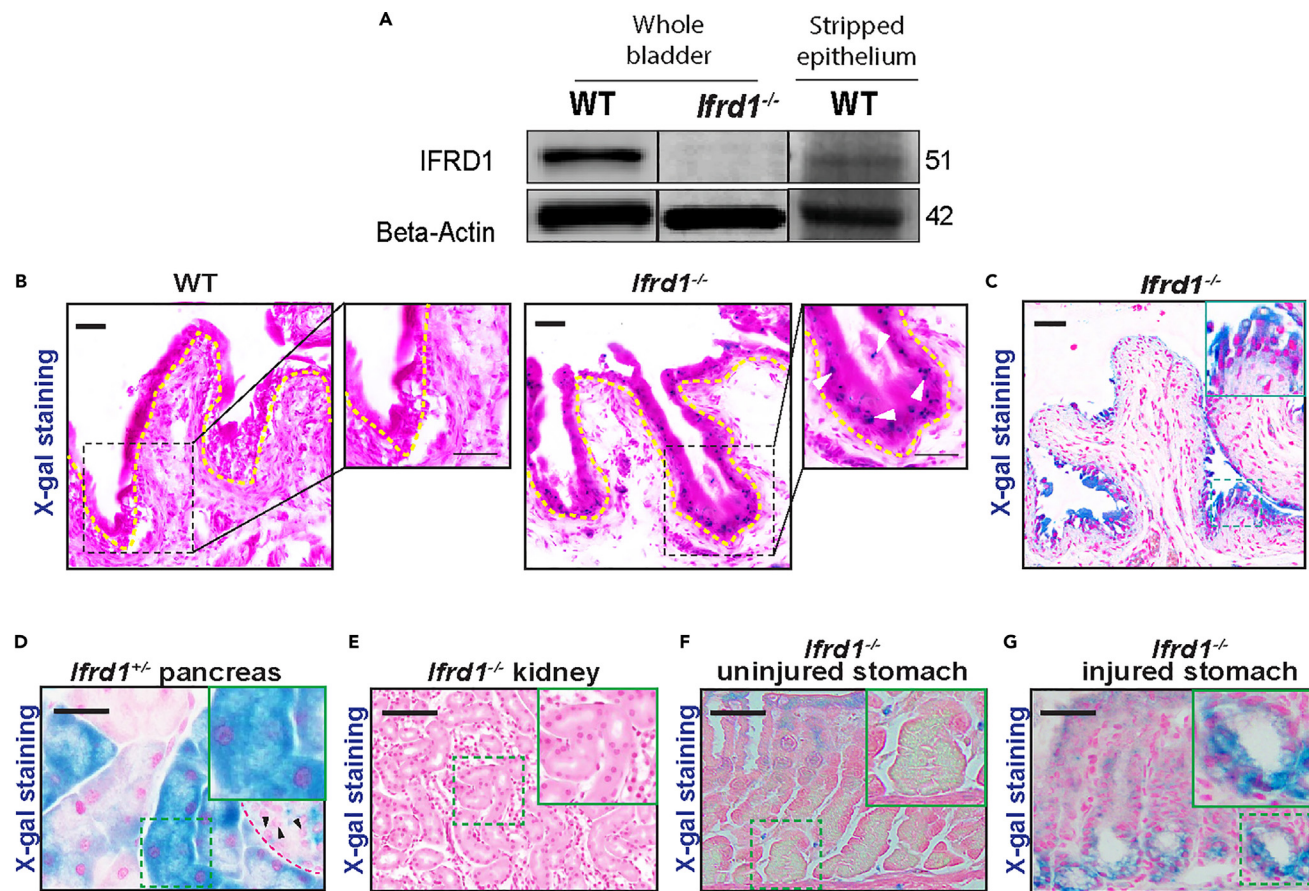
Figure 1. IFRD1 is expressed in the urothelium at homeostasis

(A) Western blot (WB) of wild-type (WT), *Ifrd1* null (*Ifrd1*$^{-/-}$) bladders and the WT stripped epithelia at homeostasis. Beta-actin serves as a housekeeping control.

(B) X-gal staining of WT bladder to detect IFRD1 expression through β-galactosidase activity in the OCT-frozen bladder sections revealing no LacZ stain in the WT urothelium (left panel) and positive LacZ stain (IFRD1-β-galactosidase expression) (right panel; white arrowheads) in the *Ifrd1*$^{-/-}$ urothelium (*n* = 3/group). Scale bar, 50 μm.

(C) X-gal staining following whole *Ifrd1*$^{-/-}$ bladder fixation revealing IFRD1-β-galactosidase expression along the urothelium in an "unperturbed" state. Scale bar, 50 μm.

(D) X-gal staining following whole *Ifrd1*$^{+/-}$ pancreas fixation revealing a robust IFRD1-β-galactosidase expression in the pancreatic acini at homeostasis (black arrowheads point the negative islets). Scale bar, 50 μm.

(E) X-gal staining following whole *Ifrd1*$^{-/-}$ kidney fixation revealing no IFRD1-β-galactosidase expression at homeostasis. Scale bar, 50 μm.

(F) X-gal staining following whole untreated *Ifrd1*$^{-/-}$ stomach fixation revealing no IFRD1-β-galactosidase expression at homeostasis. Scale bar, 50 μm.

(G) X-gal staining following whole high dose tamoxifen injured *Ifrd1*$^{-/-}$ stomach fixation revealing an induction of IFRD1-β-galactosidase expression in chief cells at the gland base. Scale bar, 50 μm.

census of these endolysosomes within the *Ifrd1*$^{-/-}$ superficial cells (Figures 2E and 2D images 2 and 4, blue circles).

Given that the *Ifrd1*$^{-/-}$ superficial cells displayed an overabundance of endolysosomes indicating a potential shift in uroplakin trafficking, we wanted to test whether loss of IFRD1 affected uroplakin trafficking. As expected, uroplakin III (UPIII) staining in the WT was expressed along the apical surface of the urothelium (Figure 2F, left panel). In contrast, uroplakins were diffusely distributed within superficial urothelial cells in *Ifrd1*$^{-/-}$ bladders (Figure 2F, right panel), suggesting aberrant uroplakin trafficking. Accordingly, transcripts encoding UPIII were significantly decreased in *Ifrd1*$^{-/-}$ bladders (Figure 2G). Consistent with these observed changes in protein trafficking, we also noted

evidence of reticulophagy (degradation of the endoplasmic reticulum via autophagy; Figure S2). Together, these findings demonstrate that loss of IFRD1 is associated with significant cellular and molecular alterations, resulting in gross defects in the urothelial ultrastructure even in an unperturbed state.

IFRD1 interacts with mRNA-translation-regulating proteins, and its absence is associated with global translational changes and enhanced ER stress

To identify the molecular partners that IFRD1 may be affecting or interacting with in the urothelium, we performed proteomic analysis of IFRD1 in the urothelial cell line 5637 (ATCC). Derived from human urothelial carcinoma, the 5637 cells maintain properties

Figure 2. Loss of IFRD1 causes alterations in urothelial cellular architecture and molecular pathways

(A) Heatmap of the global tissue transcriptome of WT and $Ifrd1^{-/-}$ bladders with fold change >1.5 and Benjamini-Hochberg FDR-adjusted $p < 0.05$ ($n = 4$ bladders/group).

(B) GSEA Hallmark pathway analysis showing significantly upregulated pathways in the WT versus $Ifrd1^{-/-}$ (blue bars) and $Ifrd1^{-/-}$ versus WT (red bars) bladders below FDR threshold of 0.25.

(C) H&E staining shows vesicles in WT (highlighted in black circles) and accumulated vesicles in $Ifrd1^{-/-}$ bladders in the superficial cells. Scale bar, 50 μm.

(D) Transmission electron microscopy (TEM) of superficial cells show MVB (red arrows) in WT and $Ifrd1^{-/-}$. $Ifrd1^{-/-}$ show accumulation of endolysosomes (white arrows). Magnified insets show the endolysosomes. Blue circles highlight the endolysosomes. Scale bar, 2 μm.

(E) Analysis of number of endolysosomes per cross-section per 100 μm² in WT and $Ifrd1^{-/-}$ superficial cells ($n = 40–97$ TEM images/group from 2 WT mice and 3 $Ifrd1^{-/-}$ mice; data shown as mean (±SEM); p value by Mann-Whitney test).

(F) Immunostaining of UPK3A (green) in WT and $Ifrd1^{-/-}$ superficial cell layer ($n = 6$ bladders/group). Magnified insets highlight the apical staining pattern in superficial cell in the WT versus diffused staining pattern in the $Ifrd1^{-/-}$. Scale bar, 50 μm.

(G) Real-time quantitative PCR (RT-qPCR) analysis of $Upk3a$ transcripts in WT and $Ifrd1^{-/-}$ bladders ($n = 9$ bladders/group; data shown as mean (±SD); p value by Mann-Whitney test).

of urothelial cells and are routinely used to represent urothelial cells.[37–40] This human urothelial cell line not only facilitated our screen for the IFRD1 interactome but also is a first step in potential translation of our *in vivo* mouse bladder study to humans. We performed co-immunoprecipitation followed by tandem mass spectrometry (MS/MS) in the 5637 cells using IFRD1 antibody and non-specific immunoglobulin G (IgG) antibody control (Figure 3A). We identified a total of 2,271 proteins that interacted with IFRD1 or the IgG control at a probability rate of over 95%. Of those 2,271 protein hits, 444 were detected in precipitates using IgG alone, 943 using IFRD1 alone, and 884 were found in both IFRD1 and IgG precipitates (Figure 3B). For our analysis, we

focused on the hits that exclusively interacted with IFRD1. The 943 IFRD1-only hits were ranked using their total spectrum count. We then selected the interactors with two or more unique peptides and FDR <0.05. This resulted in a total of 584 unique proteins (Figure 3C). These proteins were then subjected to PANTHER Overrepresentation test for GO molecular function.[41] Excitingly, a large number of these proteins were found to be enriched in regulating mRNA translation (e.g., eukaryotic translation initiation factors [eIFs], mRNA binding proteins, pre-ribosome binding factors) (Figure 3C). These molecular findings, together with our cellular observations of accumulated endolysosomes, suggested that IFRD1 might affect protein translation.
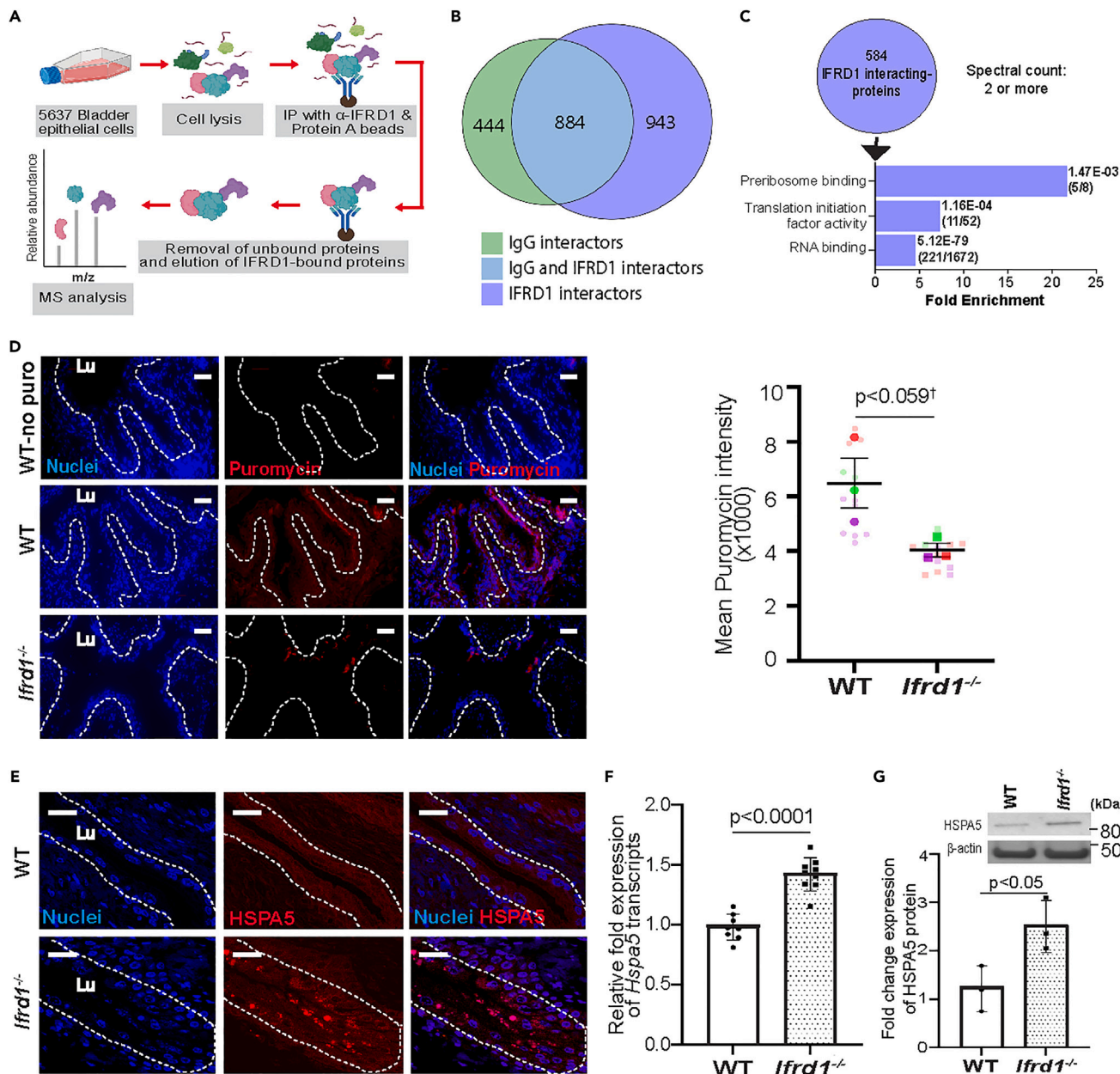
Figure 3. IFRD1 interacts with mRNA-translation-regulating proteins, and its absence is associated with global translational changes and enhanced ER stress

(A) Schematic diagram of co-immunoprecipitation of IFRD1 with tandem mass spectrometry analysis in the 5637 bladder epithelial cell line.

(B) Venn diagram shows the relationship of the protein interactors between IgG antibody control and IFRD1 pulldowns.

(C) Fold enrichment plot of the GO molecular functions of a subset of IFRD1 interactors with two or more spectral counts. FDR values and fraction (in parentheses) indicated are of those that matched with the reference list in PANTHER database.

(D) Immunostaining of bladders shows the expression of puromycin (red) in WT and $Ifrd1^{-/-}$ urothelium ("WT-no puro" represents the negative control where mice did not receive puromycin treatment prior to freezing). Nuclei are stained with DAPI (blue) (n = 3 mice/group). Quantitation of puromycin signal intensity (n = 3 bladders/group, [†]: data shown as mean (±SEM); mean of means shows p slightly >0.05 due to WT mouse-to-mouse variance; however, analysis of total ROI distribution for each genotype has p < 0.0001, p value by Mann-Whitney test). Scale bar, 20 μm.

(E) Immunostaining of HSPA5 (red) in WT and $Ifrd1^{-/-}$ urothelium. Nuclei are stained with DAPI (blue) (n = 3/group). Scale bar, 50 μm.

(F) RT-qPCR analysis of $Hspa5$ transcripts (n = 8 WT, 9 $Ifrd1^{-/-}$ bladders, data shown as mean (±SD); p value by Mann-Whitney test).

(G) WB and densitometric quantitation of HSPA5 protein levels. Beta-actin serves as a housekeeping control (n = 3/group; data shown as mean (±SD); p value by Mann-Whitney test).
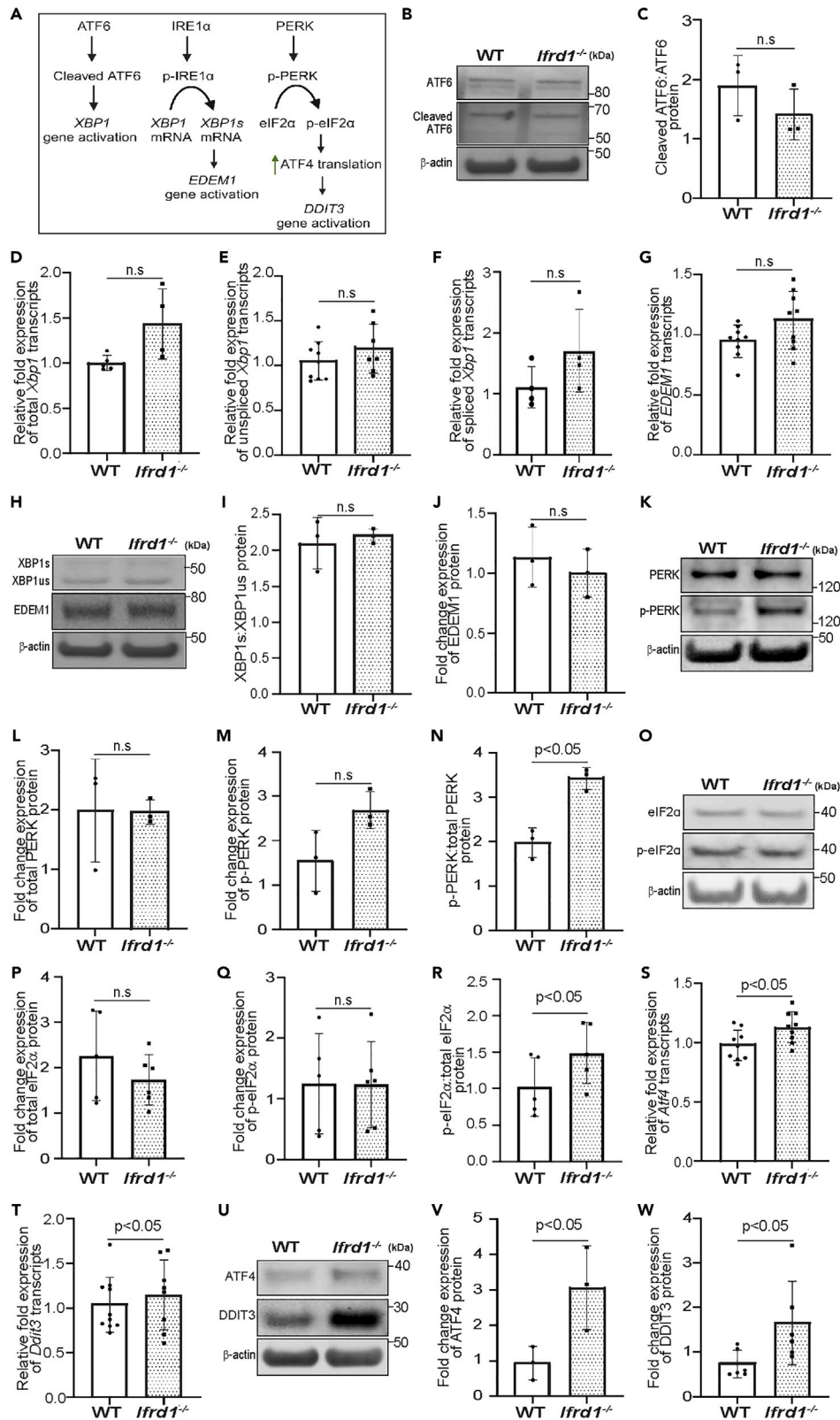
(legend on next page)

To test whether the loss of IFRD1 would influence global protein translation levels in the bladder, we performed the SunSET (surface sensing of translation) assay utilizing puromycin, an inhibitor of translation elongation, that can measure changes to protein synthesis *in vivo*, as it incorporates into elongating polypeptide chain and induces translation termination.[42] We injected WT and *Ifrd1*⁻/⁻ mice with puromycin for 2 h to allow the incorporation of puromycin into actively translating polypeptides. Subsequent immunofluorescence analysis showed that global translation in the *Ifrd1*⁻/⁻ urothelium was decreased versus WT bladders (Figure 3D).

Protein translation is a tightly regulated process in the maintenance of proteostasis, and alterations are associated with an overabundance of abnormal, misfolded proteins within the ER, leading to an ER stress response. To test whether such ER stress response is associated with the observed changes in translation levels in *Ifrd1*⁻/⁻ bladders, we first investigated levels of the ER chaperone, BiP (HSPA5), which is upregulated under conditions of ER stress. We found that the *Ifrd1*⁻/⁻ urothelium showed increased BiP in superficial cells (Figure 3E), and BiP abundance in *Ifrd1*⁻/⁻ bladders was increased at both transcript (Figure 3F) and protein level (Figure 3G). Thus, the results revealed that IFRD1 interacts with proteins involved in RNA translation, and *Ifrd1*⁻/⁻ bladders display decreased global protein translation and enhanced ER stress response.

Enhanced ER stress associated with loss of IFRD1 is linked with activation of the PERK arm of the UPR pathway

Next, we sought to determine how IFRD1 affected the ER stress response. ER stress can be induced via the unfolded protein response (UPR) activated by three ER-transmembrane, upstream stress sensors: ATF6 (activating transcription factor 6), IRE1α (inositol-requiring enzyme 1α), and PERK (protein kinase R-like endoplasmic reticulum kinase).[43,44] Under homeostatic conditions, BiP is bound to the ER-transmembrane stress sensors proteins, rendering these proteins inactive.[43,44] However, when unfolded, ER-associated proteins can bind BiP, dissociating BiP from the sensors. Each sensor, once no longer BiP-bound, then can activate its signature pattern of downstream gene expression changes (schematized in Figure 4A).

We systematically examined the impact of loss of IFRD1 on each of the arms of the UPR by analyzing the signature downstream targets. First, we examined ATF6, which when released from BiP, translocates to the Golgi where it is cleaved to release its N-terminal active form, ATF6-N (cleaved ATF6).[45] We determined abundance of total (p90) and cleaved (p50) ATF6. We saw no significant ATF6 activation in *Ifrd1*⁻/⁻ bladders (Figures 4B and 4C). RT-qPCR analysis of its downstream transcriptional target, *Xbp1*, similarly showed no significant increase in expression (Figure 4D).

Next, we determined the impact of loss of function of IFRD1 on IRE1α, which, upon release of BiP, homodimerizes and autophosphorylates, leading to induction of its RNase activity to splice the *Xbp1* unspliced mRNA (*Xbp1us*) to *Xbp1* spliced mRNA (*Xbp1s*), an active form that encodes the XBP1 protein isoform that can translocate into the nucleus to induce expression of genes such as *Edem1*.[46] We analyzed the levels of *Xbp1us* and *Xbp1s* variants' transcript and protein levels via RT-qPCR (Figures 4E and 4F) and western blot (Figures 4H, top and 4I), respectively, and saw no significant increase in *Ifrd1*⁻/⁻ bladders, consistent with IRE1α signaling not being IFRD1-dependent. Further, the XBP1s gene target, *Edem1*, also showed no significant increase in transcript (Figure 4G) or protein (Figures 4H, middle and 4J) abundance in mouse bladders lacking IFRD1 in comparison with WT.

Finally, we determined whether IFRD1 affects the PERK arm, which similarly to IRE1α, homodimerizes and autophosphorylates upon BiP release. Activated PERK then phosphorylates a protein that regulates translation initiation, eIF2α.

Figure 4. Enhanced ER stress associated with loss of IFRD1 is linked with activation of the PERK arm of the UPR pathway

(A) The three arms of unfolded protein response.

(B) WB of full-length and cleaved ATF6 proteins in WT and *Ifrd1*⁻/⁻ bladders. Beta-actin was used as a loading control.

(C) Densitometric quantitation of the ratio of cleaved ATF6 to total ATF6 protein levels (*n* = 3/group; data shown as mean (±SD); *p* values by Mann-Whitney test).

(D) RT-qPCR analysis of total *Xbp1* transcript levels (*n* = 5 WT, 4 *Ifrd1*⁻/⁻ bladders; data shown as mean (±SD); *p* values by Mann-Whitney test).

(E) RT-qPCR analysis of *Xbp1us* (unspliced) transcript levels (*n* = 8 WT, 7 *Ifrd1*⁻/⁻ bladders; data shown as mean (±SD); *p* values by Mann-Whitney test).

(F) RT-qPCR analyses of *Xbp1s* (spliced) transcript levels (*n* = 4/group; data shown as mean (±SD); *p* values by Mann-Whitney test).

(G) RT-qPCR analyses of *Edem1* transcript levels (*n* = 9/group; data shown as mean (±SD); *p* values by Mann-Whitney test).

(H) WB of XBP1s, XBP1us, and EDEM1 proteins in WT and *Ifrd1*⁻/⁻ bladders. Beta-actin was used as a loading control. (Note that the same blot has been used to probe HSPA5 in Figure 3G and hence uses the same loading control).

(I) Densitometric quantitation of the ratio of XBP1s to XBP1us protein levels (*n* = 3/group; data shown as mean (±SD); *p* values by Mann-Whitney test).

(J) Densitometric quantitation of EDEM1 protein levels (*n* = 3/group; data shown as mean (±SD); *p* values by Mann-Whitney test).

(K) WB of PERK and p-PERK proteins in WT and *Ifrd1*⁻/⁻ bladders. Beta-actin was used as a loading control.

(L) Densitometric quantitation of total PERK (*n* = 3/group; data shown as mean (±SD); *p* values by Mann-Whitney test).

(M) Densitometric quantitation of p-PERK (*n* = 3/group; data shown as mean (±SD); *p* values by Mann-Whitney test).

(N) Densitometric quantitation of the ratio of p-PERK to PERK (*n* = 3/group; data shown as mean (±SD); *p* values by Mann-Whitney test).

(O) WB of eIF2α and *p*-eIF2α proteins in WT and *Ifrd1*⁻/⁻ bladders. Beta-actin was used as a loading control.

(P) Densitometric quantitation of total eIF2α (*n* = 5/group; data shown as mean (±SD); *p* values by Mann-Whitney test).

(Q) Densitometric quantitation of *p*-eIF2α (*n* = 5/group; data shown as mean (±SD); *p* values by Mann-Whitney test).

(R) Densitometric quantitation of the ratio of *p*-eIF2α to eIF2α (*n* = 5/group; data shown as mean (±SD); *p* values by Mann-Whitney test).

(S) RT-qPCR analysis of *Atf4* transcript levels (*n* = 9/group; data shown as mean (±SD); *p* values by Mann-Whitney test).

(T) RT-qPCR analysis of *Ddit3* transcript levels (*n* = 10 WT, 8 *Ifrd1*⁻/⁻ bladders; data shown as mean (±SD); *p* values by Mann-Whitney test).

(U) WB of ATF4 and DDIT3 proteins in WT and *Ifrd1*⁻/⁻ bladders. Beta-actin was used as a loading control.

(V) Densitometric quantitation of ATF4 (*n* = 3/group; data shown as mean (±SD); *p* values by Mann-Whitney test).

(W) Densitometric quantitation of DDIT3 (*n* = 6/group; data shown as mean (±SD); *p* values by Mann-Whitney test).
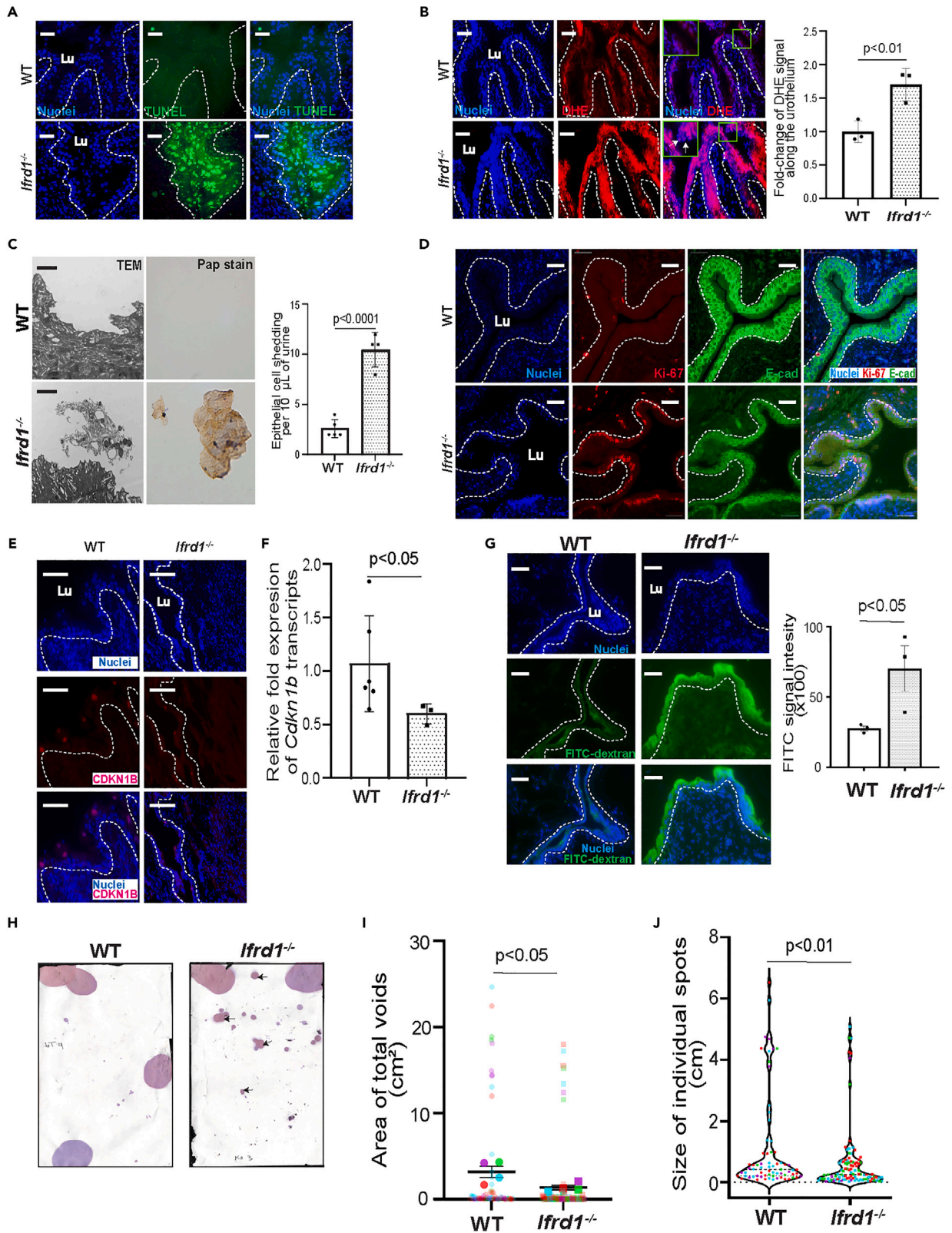
(legend on next page)

Phosphorylated eIF2α decreases activity of the eIF2 ternary complex (eIF2-GTP-tRNAi) that is required for the translation initiation.[47,48] Consistent with the PERK arm being activated by loss of IFRD1, we observed a significant increase in the ratio of phosphorylated to total PERK in the $Ifrd1^{-/-}$ bladders compared to that of WT bladders (Figures 4K–4N). If PERK were activated in the absence of IFRD1, we would also expect an increase in the phosphorylation of p-PERK target, eIF2α. Indeed, our western blot analysis revealed a significant increase in the ratio of phosphorylated to total eIF2α protein levels (Figures 4O–4R). p-PERK phosphorylation of eIF2α leads to global protein translation suppression while favoring translation of select transcripts such as $Atf4$, which induces expression of genes like $Chop$ ($Ddit3$).[43,44,49] Accordingly, both $Atf4$ and its target $Chop$ were upregulated significantly at both transcript and protein level (Figures 4S–4W) in the $Ifrd1^{-/-}$ bladders. Together, our results indicate that loss of IFRD1 in mouse bladder specifically affects the activation of PERK arm of the UPR, which may be a mediator of the urothelial stress response.

$Ifrd1^{-/-}$ mice display increased urothelial cell death, dysregulated renewal, compromised barrier integrity, and aberrant voiding behavior

We wondered whether there would be physiological relevance of the observed UPR activation of PERK-ATF4-CHOP pathway in $Ifrd1^{-/-}$ bladders. As unresolved stress can lead to persistent activation of CHOP, which can in turn lead to apoptosis when stress is not resolved, we examined whether the $Ifrd1^{-/-}$ urothelial cells exhibit increased apoptosis. To that end, the TUNEL assay was used, in which fluorescently labels cells positive for double-stranded DNA breaks that are generated during continued cells stress and apoptosis showed near universal positivity in $Ifrd1^{-/-}$ mice with rare to no positive cells in WT bladder (Figure 5A). Persistent ER stress/cell death is associated upstream and downstream with increase in ROS. To test whether this is true for $Ifrd1^{-/-}$ bladders, we stained the urothelium with the ROS indicator dye dihydroethidium (DHE), which showed stronger staining as corroborated by the higher fluorescence intensity in $Ifrd1^{-/-}$ bladders (Figure 5B). We next examined if the constitutively enhanced ROS and apoptosis levels altered the urothelial tissue homeostasis in $Ifrd1^{-/-}$ bladders. TEM images (Figure 5C, TEM)

and cytological examination of urines (Figure 5C, Pap stain) from WT and $Ifrd1^{-/-}$ mice revealed a significant level of spontaneously shed epithelial cells in $Ifrd1^{-/-}$ urine samples. Quantification of the shed cells by Pap stain revealed about 4-fold increase in the $Ifrd1^{-/-}$ urine samples at baseline, indicating that loss of IFRD1 is associated with a significantly higher urothelial cell shedding.

Under homeostatic conditions, the virtually quiescent urothelium contains few proliferatively active cells, which reside within the basal cell compartment.[4,8,9,50,51] Urothelial shedding in response to unmitigated ROS could represent a stunted response to repair damaged/stressed cells, which often leads to compensatory proliferation in the basal cell layer of the $Ifrd1^{-/-}$ urothelium. As expected, we found that WT bladders contained only scattered Ki67-positive cells (Figure 5D, top). However, within the $Ifrd1^{-/-}$ urothelium, we found increased expression of Ki67 (Figure 5D, bottom). Additionally, E-Cadherin staining, which typically labels cell-cell junctions in basal and intermediate urothelial cells, was reduced in the $Ifrd1^{-/-}$ urothelium, further indicating that urothelial integrity is constitutively compromised in these mice (Figure 5D).

Normally, increased proliferation of basal cells fuels subsequent differentiation of these cells to regenerate superficial cells. Surprisingly, however, expression of p27KIP1 (CDKN1B), a marker for terminally differentiated superficial cells, was decreased in p27kip1+ superficial cell nuclei in the $Ifrd1^{-/-}$ urothelium (Figure 5E), and $p27kip1$ transcript abundance was also decreased overall in $Ifrd1^{-/-}$ bladders (Figure 5F). These observations suggest that the loss of IFRD1 at homeostasis is not only linked to increased ER stress response and cell death but also with impaired regeneration of superficial cells.

To determine whether the absence of IFRD1 would affect barrier integrity of the urothelium, we transurethrally injected mice with FITC-dextran[52] and observed significant increase in FITC-dextran infiltration/retention in the urothelium of $Ifrd1^{-/-}$ mice (Figure 5G). This result suggests compromised urothelial structure and function that may lead to seepage of waste and toxic molecules from the urine into the bladder tissue. Compromised barrier integrity may also impact the micturition pattern/frequency of urine expulsion, which can serve as protective mechanism to eliminate waste products, maintain fluid balance, and prevent infection.[53,54] Therefore, we next sought to examine the

Figure 5. $Ifrd1^{-/-}$ mice display increased urothelial cell death, dysregulated renewal and aberrant voiding behavior

(A) TUNEL staining (green) of WT and $Ifrd1^{-/-}$ urothelial cells. Nuclei are stained with DAPI (blue) ($n = 3$/group). Scale bar, 100 μm.

(B) DHE staining (red) of WT and $Ifrd1^{-/-}$ urothelium. Nuclei are stained with DAPI (blue). Quantitation of DHE staining intensity ($n = 3$ bladders/group; data shown as mean (±SD); p values by unpaired t test). Scale bar, 100 μm.

(C) Representative TEM (left) and urine cytology (right) images show exfoliated bladder epithelial cells. Quantitation of exfoliated/shed epithelial cells ($n = 5$ WT, 4 $Ifrd1^{-/-}$ mice; data shown as mean (±SD); p values by unpaired t test). Scale bar, 2 μm.

(D) Immunostaining for Ki-67 (red) and E-cadherin (green) in WT and $Ifrd1^{-/-}$ urothelial cells ($n = 3$/group). Scale bar, 100 μm.

(E) Immunostaining of CDKN1B (red) in WT and $Ifrd1^{-/-}$ urothelium ($n = 3$/group). Scale bar, 50 μm.

(F) RT-qPCR analysis of $Cdkn1b$ transcripts in WT and $Ifrd1^{-/-}$ bladders ($n = 6$ WT, 3 $Ifrd1^{-/-}$ bladders; data shown as mean (±SD); p values by Mann-Whitney test).

(G) FITC-dextran permeability assay (green) in the WT and $Ifrd1^{-/-}$ urothelial cells reveal superficial cells with intracellular FITC-dextran in the $Ifrd1^{-/-}$ urothelium. Nuclei are stained with DAPI (blue) ($n = 3$/group). Quantitation of FITC-dextran staining intensity ($n = 3$ bladders/group; data shown as mean (±SD); p values by Mann-Whitney test). Scale bar, 100 μm.

(H) Representative images of WT (left) and $Ifrd1^{-/-}$ (right) void spot assay (VSA).

(I) Quantitation of the area of total voids from the VSA. Each dark dot is the average area of all the individual voids that are depicted as transparent dots of the same color. ($n = 4$/group, data shown as mean (±SEM), p values by unpaired t test).

(J) Quantitation of the size of all the individual spots from the VSA. All the data points from one mouse are presented in one color. (Data represented as interquartile range of size distribution where the central line represents the median (±SD), $n = 4$/group, p values by unpaired t test).

voiding behavior of the WT and *Ifrd1*$^{-/-}$ mice using the spontaneous void spot assay (VSA), a widely employed tool for assessing micturition in experimental mice.[55–57] When placed on a filter paper, mice typically seek edges to urinate (Figure 5H, WT). However, *Ifrd1*$^{-/-}$ mice voided all along the filter paper and on the edges (Figure 5H, black arrows). Measurement of the urine-covered area (Figure 5I) and the size of individual voids (Figure 5J) revealed that most void spots from *Ifrd1*$^{-/-}$ mice were smaller (Figures 5I and 5J). Furthermore, despite the increase in the number of voids, the total covered area was less, suggesting that *Ifrd1*$^{-/-}$ mice exhibit incontinence/voiding dysfunction.

DISCUSSION

The urothelium is remarkable in its flexibility and impermeability. Injury such as that induced by infection or mechanical/chemical stressors in the tissue results in rapid epithelial exfoliation and renewal and restoration of homeostasis. In the current study, we identify that the transcription factor IFRD1 plays a role in preventing spontaneous induction of the bladder injury response. IFRD1 has been shown to be expressed in bladder in bulk and scRNA-seq studies[58,59] but hitherto largely been studied in other tissues for its role in response to cell injury. Here, we show that the mouse bladder, particularly the urothelium, not only expresses IFRD1 at homeostasis but also that its loss is associated with alterations in urothelial morphology and function. We show that IFRD1 associates with proteins involved in protein translation, and *Ifrd1*$^{-/-}$ bladders/urothelium had reduced global translation with concomitant activation of the ER stress response. ER stress in the absence of IFRD1 was linked to activation of the PERK arm of UPR, and the *Ifrd1*$^{-/-}$ bladders exhibited increased oxidative stress, cell death and reduced terminal differentiation, enhanced permeability, and aberrant voiding behavior. Thus, our work suggests that even homeostatic activity of the bladder urothelium could constitute a potential "stress" situation that requires management of UPR/ER stress by proteins such as IFRD1 that are normally required only in stressful situations in other tissues.

IFRD1 is an immediate-early gene induced by a variety of signals/stresses implicated in regulation of growth and differentiation of neurons, myocytes, enterocytes,[34,60–62] and elevated levels of IFRD1 are observed in multiple acute injury models such as muscle trauma,[34,61,63] small intestine resection,[33,64] ischemia-reperfusion,[65] pelvic prolapse,[66] fat injury/stress/obesity,[25,67] and stroke,[68] highlighting a key role for IFRD1 in mediating cellular and tissue regeneration after injury. Our work on paligenosis reiterated the early activation of IFRD1 following injury, and its absence led to decreased regeneration and increased cell death in diverse organs such as stomach, liver, kidney, and pancreas in mice and humans.[32,69,70] Additionally, injury-induced expression of IFRD1 is found to be conserved in other organisms such as Axolotls,[32,71] *Drosophila*,[32,72,73] and *Schizosaccharomyces pombe*.[32] Given such critical roles of IFRD1 in regulating injury response, it is surprising that IFRD1 plays a seemingly steady-state role in the bladder. We speculate that perhaps the continual voiding cycles of the urinary bladder may require extensive trafficking and recycling of uroplakins that produces a consistently stressed state, requiring the urothelium to constitutively express

stress-relieving proteins. Injury is known to engage inflammatory pathways in response to stress, and a growing number of studies point to the role of UPR activation to alleviate such stress and restore homeostasis.[74,75] One crucial event in UPR activation involves the phosphorylation of Ser51 on the alpha subunit of eukaryotic translation initiation factor 2 alpha (eIF2α) that halts the production of intact 80S ribosomes essential for translation.[76–78] Instead, 40S ribosomes with mRNA and a few initiation factors (a.k.a preinitiation complex) localize to form stress granules.[79–81] This is also evident in assays of ribosome activity as a collapse of polysome peaks.[82–84] The involvement of IFRD1 in translation control, particularly concerning ribosomes, is reasonable, given its ability, along with proteins such as ATF4 or PPP1R15B, to evade the translation block induced by cellular stress.[29,85,86] Further support for a role for IFRD1 in mediating stress response via translational machinery and ribosomal activity comes from a close structurally related paralog, IFRD2, which is predicted to interfere with translation by occupying the P and E sites of the ribosome and inserting an N-terminal helix into the mRNA exit channel.[87] Furthermore, our co-immunoprecipitation data demonstrate that IFRD1 interacts with various components associated with pre-ribosomes, translation initiation, and mRNA binding, all of which are closely linked to ribosomal function. This suggests a direct interaction between IFRD1 and the ribosome, influencing the translation process. Detailed understanding of this mechanism is warranted.

In addition to translation inhibition, persistent unresolved UPR activation impairs ER functions such as protein-folding, processing, and trafficking for an extended period, which can induce apoptosis. Our results demonstrating a diffuse expression pattern and reduced expression of the uroplakin, UPK3A, along with increased TUNEL staining, support the conclusion that UPR is constitutively activated, causing both uroplakin trafficking defects in the bladders of IFRD1 null mice as well as constant pro-apoptotic signaling. We note that TUNEL simply labels DNA strand breaks, which usually correlate with—but are not entirely specific for—apoptosis. In terminally differentiated cells like those of the superficial layer of urothelium, it is possible that strand breaks accumulate as a result of ROS (which are also elevated in the absence of IFRD1) and that repair is slow in these non-dividing cells, even if they are not all targeted for eventual death. We also noticed not only decreased p27kip1 in the bladder in the absence of IFRD1 but also a diffuse, intracellular distribution of this normally nuclear protein, suggesting altered proteostasis of this protein as well as decreased differentiation. The increased ROS and other aberrant cellular features correlated with epithelial cell shedding in the urine of *Ifrd1*$^{-/-}$ mice. Moreover, we notice that the frequent shed cells in these mice had smaller nuclei than those of WT, suggesting that some of these shed *Ifrd1*$^{-/-}$ cells were less differentiated intermediate cells, which are not normally seen in urine. Urine usually contains only rare shed superficial cells, unless the bladder encounters stresses such as infection.[8,88,89] Thus, *Ifrd1*$^{-/-}$ mice may display cell death and shedding of cells even prior to terminal differentiation, correlating with the reduction in p27kip1 staining and expression. Moreover, our *in vivo* assessment using the FITC-Dextran assay demonstrated heightened permeability of the urothelial barrier in the bladder. This observation aligns

with the dysregulated turnover of superficial cells and altered patterns of micturition, as confirmed by our void spot assay.

The increased shedding and other cellular abnormalities in $Ifrd1^{-/-}$ mice are reminiscent of recent work[59] from our group demonstrating that aged bladders (>15 months of age) show enhanced DNA damage, increased ROS, and higher levels of epithelial shedding at homeostasis. Other studies have also linked these phenotypes with aging and lower urinary tract dysfunction.[90,91] Indeed, we and others have shown that the aging urothelium is associated with alterations to endolysosomal content[59,92] that is seen in $Ifrd1^{-/-}$ superficial cells. In other words, loss of IFRD1 might trigger an aging-like phenotype. It may be that these effects noted in aging are partly mediated via the functions of IFRD1 and its association with translation, ER stress, and UPR activation. Consistent with this, bulk RNA-seq analysis of young versus aged bladders indicated aging-associated reduction in IFRD1 expression.[59] Whether reduced IFRD1 expression with aging might suggest a molecular basis for the aging phenotype is an important avenue to investigate. Further, whether any of these alterations are mediated via changes in urothelial-stromal signaling remains to be explored. Additionally, IFRD1 has been shown to exert some of its effects via modulation of transcriptional activity via its interaction with histone deacetylases (HDACs), and its altered expression is associated with loss of polarity in epithelial cells via its interaction with the HDACs.[93–95] Indeed, our MS/MS analysis revealed IFRD1 interaction with HDACs (HDAC4 and SIRT6, *data not shown*) in the urothelium. As altered polarity in the epithelial cells is linked with lower E-cadherin expression and cancer including bladder cancer,[96] we could speculate that alterations to the E-cadherin levels we note in the urothelium upon loss of IFRD1 may have a more profound impact as the mice get older.

Our work here suggests that the seemingly quiescent urothelium may be in fact under a constant state of stress owing to the massive structural transitions it undergoes daily during normal voiding activity. Loss of IFRD1 appears to alter voiding dynamics. Although our limited observations do not explain why or how, it is nevertheless striking that stress urinary incontinence (SUI) and pelvic organ prolapse (POP), conditions associated with voiding dysfunction have been linked to ER stress, and POP has even been correlated with altered IFRD1 expression in women.[66,97] Specifically, postmenopausal women with SUI have shown an activated PERK arm of the UPR with no changes to IRE1α or ATF6 arms, resembling the phenotype observed in IFRD1 null mice from our study.[97] Additionally, this study showed that increased apoptosis mediated by PERK-ATF4-CHOP correlates with the SUI in postmenopausal women. Similarly, *IFRD1* mRNA levels were altered in POP tissues compared to controls in modulating the pathogenesis of POP.[66] Given our findings that IFRD1 plays a key role in modulating the ER stress response and maintaining the urothelial homeostasis correlates with a physiologically relevant phenotype that is reproduced in women with bladder dysfunction, studies are warranted to determine the involvement of aberrant UPR in POP-SUI pathology. Delineating the sequence of events leading up to SUI pathology may highlight importance of IFRD1 as a potential target for diagnosis and/or therapy for bladder dysfunction.[98]

Overall, our findings suggest that IFRD1 plays a critical role in maintenance of urothelial structure and bladder functions at homeostasis, and its loss is associated with alterations to proteostasis and impaired superficial cell renewal with pathophysiologic results on bladder function. Understanding the mechanisms of action of IFRD1 may shed light on urothelial homeostatic activities that are altered in the aged or injured/infected/diseased bladders.

Limitations of the study

Our study characterizes IFRD1 in the bladder and its functional role in the urothelium. However, we did not use a urothelium-specific *Ifrd1* knockout mouse model. Utilization of urothelial-specific *Ifrd1* knockout model in future work will allow us to further dissect the role of IFRD1 in mediating the aforementioned phenotypes that validate the role of IFRD1 as a key player in maintenance of bladder health. Nevertheless, our findings that IFRD1 is expressed at homeostasis in the urothelium, and the observed phenotypes associated with urothelial structure and function, are sufficient to support its role in maintaining the urothelial integrity and, in turn, bladder function.

RESOURCE AVAILABILITY

Lead contact
Further information and requests for resources and reagents should be directed to and will be fulfilled by the Lead contact, Indira U. Mysorekar (indira.mysorekar@bcm.edu).

Materials availability
This study did not generate new unique reagents.

Data and code availability
- This study did not generate new and original code.
- Data are deposited at the Gene Expression Omnibus and The ProteomeXchange Consortium and publicly available as of the date of publication. Accession numbers are listed in the key resources table.
- Any additional information required to reanalyze the data reported in this paper is available from the lead contact upon request.

AUTHOR CONTRIBUTIONS

B.E.F., A.K.R., A.M.S., C.J.C., J.C.M., and I.U.M. conceived the experimental plan; B.E.F. and A.K.R. performed most experiments assisted by A.M.S., R.C., S.B., C.J.C. J.W.B. and C.J.C. provided expertise. B.E.F., A.K.R., A.M.S., J.C.M., and I.U.M. wrote the manuscript, and all authors approved the final draft.

DECLARATION OF INTERESTS

I.U.M. serves on the scientific advisory board of Seed Health. No conflicts of interest exist.

STAR★METHODS

Detailed methods are provided in the online version of this paper and include the following:

- KEY RESOURCES TABLE
- EXPERIMENTAL MODEL AND STUDY PARTICIPANT DETAILS
  - Mice
  - Mouse genotyping
- METHOD DETAILS
  - Cell lines
  - Immunofluorescence
  - X-gal staining
  - *In vivo* permeability assay
  - H&E staining
  - Transmission electron microscopy (TEM) and quantification of cell structures
  - TUNEL and SunSET assays
  - Urine cytology
  - *In vivo* ROS assay and imaging
  - Void spot assay (VSA)
  - Co-immunoprecipitation and proteomic analysis
  - RNA-sequencing
  - Real-time quantitative PCR (RT-qPCR)
  - Stripped bladder epithelium
  - Western blotting
- QUANTIFICATION AND STATISTICAL ANALYSIS

SUPPLEMENTAL INFORMATION

Supplemental information can be found online at https://doi.org/10.1016/j.isci.2024.111282.

REFERENCES

1. Rajasekaran, M., Stein, P., and Parsons, C.L. (2006). Toxic factors in human urine that injure urothelium. Int. J. Urol. *13*, 409–414.

2. Hicks, R.M., Ketterer, B., and Warren, R.C. (1974). The ultrastructure and chemistry of the luminal plasma membrane of the mammalian urinary bladder: a structure with low permeability to water and ions. Philos. Trans. R. Soc. Lond. B Biol. Sci. *268*, 23–38. https://doi.org/10.1098/rstb.1974.0013.

3. Jost, S.P. (1989). Cell cycle of normal bladder urothelium in developing and adult mice. Virchows Arch. B Cell Pathol. *57*, 27–36.

4. Jost, S.P., and Potten, C.S. (1986). Urothelial Proliferation In Growing Mice. Cell Tissue Kinet. *19*, 155–160.

5. Colopy, S.A., Bjorling, D.E., Mulligan, W.A., and Bushman, W. (2014). A population of progenitor cells in the basal and intermediate layers of the murine bladder urothelium contributes to urothelial development and regeneration. Dev. Dynam. *243*, 988–998.

6. Gandhi, D., Molotkov, A., Batourina, E., Schneider, K., Dan, H., Reiley, M., Laufer, E., Metzger, D., Liang, F., Liao, Y., et al. (2013). Retinoid Signaling in Progenitors Controls Specification and Regeneration of the Urothelium. Dev. Cell *26*, 469–482.

7. Mulvey, M.A., Lopez-Boado, Y.S., Wilson, C.L., Roth, R., Parks, W.C., Heuser, J., and Hultgren, S.J. (1998). Induction and evasion of host defenses by type 1-piliated uropathogenic Escherichia coli. Science *282*, 1494–1497.

8. Mysorekar, I.U., Mulvey, M.A., Hultgren, S.J., and Gordon, J.I. (2002). Molecular regulation of urothelial renewal and host defenses during infection with uropathogenic Escherichia coli. J. Biol. Chem. *277*, 7412–7419.

9. Mysorekar, I.U., Isaacson-Schmid, M., Walker, J.N., Mills, J.C., and Hultgren, S.J. (2009). Bone morphogenetic protein 4 signaling regulates epithelial renewal in the urinary tract in response to uropathogenic infection. Cell Host Microbe *5*, 463–475.

10. Romih, R., Koprivec, D., Martincic, D.S., and Jezernik, K. (2001). Restoration of the rat urothelium after cyclophosphaheximide after treatment. Cell Biol. Int. *25*, 531–537.

11. Hyuga, T., Fujimoto, K., Hashimoto, D., Tanabe, K., Kubo, T., Nakamura, S., Ueda, Y., Fujita-Jimbo, E., Muramatsu, K., Suzuki, K., et al. (2023). Wound healing responses of urinary extravasation after urethral injury. Sci. Rep. *13*, 10628.

12. Jafari, N.V., and Rohn, J.L. (2022). The urothelium: a multi-faceted barrier against a harsh environment. Mucosal Immunol. *15*, 1127–1142.

13. Kreft, M.E., Sterle, M., Veranič, P., and Jezernik, K. (2005). Urothelial injuries and the early wound healing response: tight junctions and urothelial cytodifferentiation. Histochem. Cell Biol. *123*, 529–539.

14. Wang, C., Ross, W.T., and Mysorekar, I.U. (2017). Urothelial Generation and Regeneration in Development, Injury, and Cancer. Dev. Dynam. *246*, 336–343.

15. Balestreire, E.M., and Apodaca, G. (2007). Apical epidermal growth factor receptor signaling: regulation of stretch-dependent exocytosis in bladder umbrella cells. Mol. Biol. Cell *18*, 1312–1323.

16. Chen, Y., Guo, X., Deng, F.M., Liang, F.X., Sun, W., Ren, M., Izumi, T., Sabatini, D.D., Sun, T.T., and Kreibich, G. (2003). Rab27b is associated with fusiform vesicles and may be involved in targeting uroplakins to urothelial apical membranes. Proc. Natl. Acad. Sci. USA *100*, 14012–14017.

17. Lewis, S.A., and de Moura, J.L. (1982). Incorporation of cytoplasmic vesicles into apical membrane of mammalian urinary bladder epithelium. Nature *297*, 685–688.

18. Minsky, B.D., and Chlapowski, F.J. (1978). Morphometric analysis of the translocation of lumenal membrane between cytoplasm and cell surface of transitional epithelial cells during the expansion-contraction cycles of mammalian urinary bladder. J. Cell Biol. *77*, 685–697.

19. Truschel, S.T., Wang, E., Ruiz, W.G., Leung, S.M., Rojas, R., Lavelle, J., Zeidel, M., Stoffer, D., and Apodaca, G. (2002). Stretch-regulated exocytosis/endocytosis in bladder umbrella cells. Mol. Biol. Cell *13*, 830–846.

20. Amano, O., Kataoka, S., and Yamamoto, T.Y. (1991). Turnover of asymmetric unit membranes in the transitional epithelial superficial cells of the rat urinary bladder. Anat. Rec. *229*, 9–15.

21. Bäck, N., Rajagopal, C., Mains, R.E., and Eipper, B.A. (2010). Secretory Granule Membrane Protein Recycles through Multivesicular Bodies. Traffic *11*, 972–986.

22. Khandelwal, P., Ruiz, W.G., and Apodaca, G. (2010). Compensatory endocytosis in bladder umbrella cells occurs through an integrin-regulated and RhoA- and dynamin-dependent pathway. EMBO J. *29*, 1961–1975.

23. Zhou, G., Liang, F.X., Romih, R., Wang, Z., Liao, Y., Ghiso, J., Luque-Garcia, J.L., Neubert, T.A., Kreibich, G., Alonso, M.A., et al. (2012). MAL facilitates the incorporation of exocytic uroplakin-delivering vesicles into the apical membrane of urothelial umbrella cells. Mol. Biol. Cell 23, 1354–1366.

24. Iezaki, T., Fukasawa, K., Park, G., Horie, T., Kanayama, T., Ozaki, K., Onishi, Y., Takahata, Y., Nakamura, Y., Takarada, T., et al. (2016). Transcriptional Modulator Ifrd1 Regulates Osteoclast Differentiation through Enhancing the NF-κB/NFATc1 Pathway. Mol. Cell Biol. 36, 2451–2463.

25. Park, G., Horie, T., Kanayama, T., Fukasawa, K., Iezaki, T., Onishi, Y., Ozaki, K., Nakamura, Y., Yoneda, Y., Takarada, T., and Hinoi, E. (2017). The transcriptional modulator Ifrd1 controls PGC -1α expression under short-term adrenergic stimulation in brown adipocytes. FEBS J. 284, 784–795.

26. Tummers, B., Goedemans, R., Pelascini, L.P.L., Jordanova, E.S., van Esch, E.M.G., Meyers, C., Melief, C.J.M., Boer, J.M., and van der Burg, S.H. (2015). The interferon-related developmental regulator 1 is used by human papillomavirus to suppress NFκB activation. Nat. Commun. 6, 6537.

27. Tirone, F., and Shooter, E.M. (1989). Early gene regulation by nerve growth factor in PC12 cells: induction of an interferon-related gene 86, 2088–2092.

28. Rendleman, J., Cheng, Z., Maity, S., Kastelic, N., Munschauer, M., Allgoewer, K., Teo, G., Zhang, Y.B.M., Lei, A., Parker, B., et al. (2018). New insights into the cellular temporal response to proteostatic stress. Elife 7, e39054.

29. Zhao, C., Datta, S., Mandal, P., Xu, S., and Hamilton, T. (2010). Stress-sensitive regulation of IFRD1 mRNA decay is mediated by an upstream open reading frame. J. Biol. Chem. 285, 8552–8562.

30. Ndum, O.S. (2010). The Role of IFRD1 during the Integrated Stress Response (Case Western Reserve University).

31. Otu, H.H., Naxerova, K., Ho, K., Can, H., Nesbitt, N., Libermann, T.A., and Karp, S.J. (2007). Restoration of liver mass after injury requires proliferative and not embryonic transcriptional patterns. J. Biol. Chem. 282, 11197–11204.

32. Miao, Z.-F., Lewis, M.A., Cho, C.J., Adkins-Threats, M., Park, D., Brown, J.W., Sun, J.X., Burclaff, J.R., Kennedy, S., Lu, J., et al. (2020). A Dedicated Evolutionarily Conserved Molecular Network Licenses Differentiated Cells to Return to the Cell Cycle. Dev. Cell 55, 178–194.

33. Yu, C., Jiang, S., Lu, J., Coughlin, C.C., Wang, Y., Swietlicki, E.A., Wang, L., Vietor, I., Huber, L.A., Cikes, D., et al. (2010). Deletion of Tis7 protects mice from high-fat diet-induced weight gain and blunts the intestinal adaptive response postresection. J. Nutr. 140, 1907–1914.

34. Vadivelu, S.K., Kurzbauer, R., Dieplinger, B., Zweyer, M., Schafer, R., Wernig, A., Vietor, I., and Huber, L.A. (2004). Muscle Regeneration and Myogenic Differentiation Defects in Mice Lacking TIS7. Mol. Cell Biol. 24, 3514–3525.

35. Lewis, M.A. (2019). The Role of IFRD1 in the Recruitment and Function of Reserve Stem Cells in Regeneration and Cancer (Washington University).

36. The Jackson Laboratory. β-Galactosidase staining of frozen sections. https://www.jax.org/research-and-faculty/resources/cre-repository/fresh-frozen-slide-staining-protocol.

37. Joshi, C.S., Mora, A., Felder, P.A., and Mysorekar, I.U. (2021). NRF2 promotes urothelial cell response to bacterial infection by regulating reactive oxygen species and RAB27B expression. Cell Rep. 37, 109856.

38. Wellens, A., Garofalo, C., Nguyen, H., Van Gerven, N., Slättegård, R., Hernalsteens, J.P., Wyns, L., Oscarson, S., De Greve, H., Hultgren, S., and Bouckaert, J. (2008). Intervening with urinary tract infections using anti-adhesives based on the crystal structure of the FimH-oligomannose-3 complex. PLoS One 3, e2040.

39. Hunstad, D.A., Justice, S.S., Hung, C.S., Lauer, S.R., and Hultgren, S.J. (2005). Suppression of bladder epithelial cytokine responses by uropathogenic Escherichia coli. Infect. Immun. 73, 3999–4006.

40. Lin, A.E., Beasley, F.C., Olson, J., Keller, N., Shalwitz, R.A., Hannan, T.J., Hultgren, S.J., and Nizet, V. (2015). Role of Hypoxia Inducible Factor-1α (HIF-1α) in Innate Defense against Uropathogenic Escherichia coli Infection. PLoS Pathog. 11, e1004818.

41. Mi, H., Muruganujan, A., Huang, X., Ebert, D., Mills, C., Guo, X., and Thomas, P.D. (2019). Protocol Update for large-scale genome and gene function analysis with the PANTHER classification system (v.14.0). Nat. Protoc. 14, 703–721.

42. Schmidt, E.K., Clavarino, G., Ceppi, M., and Pierre, P. (2009). SUnSET, a nonradioactive method to monitor protein synthesis. Nat. Methods 6, 275–277.

43. Read, A., and Schröder, M. (2021). The Unfolded Protein Response: An Overview. Biology 10, 384.

44. Walter, P., and Ron, D. (2011). The unfolded protein response: from stress pathway to homeostatic regulation. Science 334, 1081–1086.

45. Haze, K., Yoshida, H., Yanagi, H., Yura, T., and Mori, K. (1999). Mammalian transcription factor ATF6 is synthesized as a transmembrane protein and activated by proteolysis in response to endoplasmic reticulum stress. Mol. Biol. Cell 10, 3787–3799.

46. Park, S.-M., Kang, T.-I., and So, J.-S. (2021). Roles of XBP1s in Transcriptional Regulation of Target Genes. Biomedicines 9, 791.

47. Gordiyenko, Y., Llácer, J.L., and Ramakrishnan, V. (2019). Structural basis for the inhibition of translation through eIF2α phosphorylation. Nat. Commun. 10, 2640.

48. Kimball, S.R., Fabian, J.R., Pavitt, G.D., Hinnebusch, A.G., and Jefferson, L.S. (1998). Regulation of guanine nucleotide exchange through phosphorylation of eukaryotic initiation factor eIF2alpha. Role of the alpha-and delta-subunits of eiF2b. J. Biol. Chem. 273, 12841–12845.

49. Nishitoh, H. (2012). CHOP is a multifunctional transcription factor in the ER stress response. J. Biochem. 151, 217–219.

50. Jost, S.P. (1986). Renewal of normal urothelium in adult mice. Virchows Arch. B Cell Pathol. Incl. Mol. Pathol. 51, 65–70.

51. Papafotiou, G., Paraskevopoulou, V., Vasilaki, E., Kanaki, Z., Paschalidis, N., and Klinakis, A. (2016). KRT14 marks a subpopulation of bladder basal cells with pivotal role in regeneration and tumorigenesis. Nat. Commun. 7, 11914.

52. Shin, K., Lee, J., Guo, N., Kim, J., Lim, A., Qu, L., Mysorekar, I.U., and Beachy, P.A. (2011). Hedgehog/Wnt feedback supports regenerative proliferation of epithelial stem cells in bladder. Nature 472, 110–114.

53. Silverman, D.T., Alguacil, J., Rothman, N., Real, F.X., Garcia-Closas, M., Cantor, K.P., Malats, N., Tardon, A., Serra, C., Garcia-Closas, R., et al. (2008). Does increased urination frequency protect against bladder cancer? Int. J. Cancer 123, 1644–1648.

54. Flores, J.L., Cortes, G.A., and Leslie, S.W. (2024). Physiology, Urination. In StatPearls (Treasure Island (FL): StatPearls Publishing).

55. Fashemi, B.E., and Mysorekar, I.U. (2018). Reflections on the void: the art of micturition analysis. Am. J. Physiol. Ren. Physiol. 315, F1446–F1448.

56. Hill, W.G., Zeidel, M.L., Bjorling, D.E., and Vezina, C.M. (2018). Void spot assay: recommendations on the use of a simple micturition assay for mice. Am. J. Physiol. Ren. Physiol. 315, F1422–F1429.

57. Wegner, K.A., Abler, L.L., Oakes, S.R., Mehta, G.S., Ritter, K.E., Hill, W.G., Zwaans, B.M., Lamb, L.E., Wang, Z., Bjorling, D.E., et al. (2018). Void spot assay procedural optimization and software for rapid and objective quantification of rodent voiding function, including overlapping urine spots. Am. J. Physiol. Ren. Physiol. 315, F1067–F1080.

58. Yu, Z., Liao, J., Chen, Y., Zou, C., Zhang, H., Cheng, J., Liu, D., Li, T., Zhang, Q., Li, J., et al. (2019). Single-Cell Transcriptomic Map of the Human and Mouse Bladders. J. Am. Soc. Nephrol. 30, 2159–2176.

59. Joshi, C.S., Salazar, A.M., Wang, C., Ligon, M.M., Chappidi, R.R., Fashemi, B.E., Felder, P.A., Mora, A., Grimm, S.L., Coarfa, C., and Mysorekar, I.U. (2024). D-Mannose reduces cellular senescence and NLRP3/GasderminD/IL-1β-driven pyroptotic uroepithelial cell shedding

in the murine bladder. Dev. Cell *59*, 33–47.e5. https://doi.org/10.1016/j.devcel.2023.11.017.

60. Arenander, A.T., Lim, R.W., Varnum, B.C., Cole, R., de Vellis, J., and Herschman, H.R. (1989). TIS gene expression in cultured rat astrocytes: induction by mitogens and stellation agents. J. Neurosci. Res. *23*, 247–256.

61. Guardavaccaro, D., Ciotti, M.T., Schäfer, B.W., Montagnoli, A., and Tirone, F. (1995). Inhibition of differentiation in myoblasts deprived of the interferon-related protein PC4. Cell Growth Differ. *6*, 159–169.

62. Wang, Y., Iordanov, H., Swietlicki, E.A., Wang, L., Fritsch, C., Coleman, T., Semenkovich, C.F., Levin, M.S., and Rubin, D.C. (2005). Targeted intestinal overexpression of the immediate early gene tis7 in transgenic mice increases triglyceride absorption and adiposity. J. Biol. Chem. *280*, 34764–34775.

63. Petrie, M.A., Suneja, M., Faidley, E., and Shields, R.K. (2014). A minimal dose of electrically induced muscle activity regulates distinct gene signaling pathways in humans with spinal cord injury. PLoS One *9*, e115791.

64. Rubin, D.C., Swietlicki, E.A., Wang, J.L., and Levin, M.S. (1998). Regulation of PC4/TIS7 expression in adapting remnant intestine after resection. Am. J. Physiol. *275*, G506–G513.

65. Nelson, D.P., Wechsler, S.B., Miura, T., Stagg, A., Newburger, J.W., Mayer, J.E., Jr., and Neufeld, E.J. (2002). Myocardial immediate early gene activation after cardiopulmonary bypass with cardiac ischemia-re-perfusion. Ann. Thorac. Surg. *73*, 156–162.

66. Zhao, Y., Xia, Z., Lin, T., and Yin, Y. (2020). Significance of hub genes and immune cell infiltration identified by bioinformatics analysis in pelvic organ prolapse. PeerJ *8*, e9773.

67. Nakamura, Y., Hinoi, E., Iezaki, T., Takada, S., Hashizume, S., Takahata, Y., Tsuruta, E., Takahashi, S., and Yoneda, Y. (2013). Repression of adipogenesis through promotion of Wnt/β-catenin signaling by TIS7 up-regulated in adipocytes under hypoxia. Biochim. Biophys. Acta *1832*, 1117–1128.

68. Roth, A., Gill, R., and Certa, U. (2003). Temporal and spatial gene expression patterns after experimental stroke in a rat model and characterization of PC4, a potential regulator of transcription. Mol. Cell. Neurosci. *22*, 353–364.

69. Radyk, M.D., Spatz, L.B., Peña, B.L., Brown, J.W., Burclaff, J., Cho, C.J., Kefalov, Y., Shih, C.C., Fitzpatrick, J.A., and Mills, J.C. (2021). ATF3 induces RAB7 to govern autodegradation in paligenosis, a conserved cell plasticity program. EMBO Rep. *22*, e51806.

70. Brown, J.W., Cho, C.J., and Mills, J.C. (2022). Paligenosis: Cellular Remodeling During Tissue Repair. Annu. Rev. Physiol. *84*, 461–483.

71. Gerber, T., Murawala, P., Knapp, D., Masselink, W., Schuez, M., Hermann, S., Gac-Santel, M., Nowoshilow, S., Kageyama, J., Khattak, S., et al. (2018). Single-cell analysis uncovers convergence of cell identities during axolotl limb regeneration. Science *362*, eaaq0681.

72. Vodovar, N., Vinals, M., Liehl, P., Basset, A., Degrouard, J., Spellman, P., Boccard, F., and Lemaitre, B. (2005). *Drosophila* host defense after oral infection by an entomopathogenic *Pseudomonas* species *102*, 11414–11419.

73. Bou Sleiman, M.S., Osman, D., Massouras, A., Hoffmann, A.A., Lemaitre, B., and Deplancke, B. (2015). Genetic, molecular and physiological basis of variation in Drosophila gut immunocompetence. Nat. Commun. *6*, 7829.

74. Schröder, M., and Kaufman, R.J. (2005). The mammalian unfolded protein response. Annu. Rev. Biochem. *74*, 739–789.

75. Zhang, K., and Kaufman, R.J. (2008). From endoplasmic-reticulum stress to the inflammatory response. Nature *454*, 455–462.

76. Teske, B.F., Wek, S.A., Bunpo, P., Cundiff, J.K., McClintick, J.N., Anthony, T.G., and Wek, R.C. (2011). The eIF2 kinase PERK and the integrated stress response facilitate activation of ATF6 during endoplasmic reticulum stress. Mol. Biol. Cell *22*, 4390–4405.

77. Pakos-Zebrucka, K., Koryga, I., Mnich, K., Ljujic, M., Samali, A., and Gorman, A.M. (2016). The integrated stress response. EMBO Rep. *17*, 1374–1395.

78. Costa-Mattioli, M., and Walter, P. (2020). The integrated stress response: From mechanism to disease. Science *368*, eaat5314.

79. Kedersha, N., Ivanov, P., and Anderson, P. (2013). Stress granules and cell signaling: more than just a passing phase? Trends Biochem. Sci. *38*, 494–506.

80. Kedersha, N.L., Gupta, M., Li, W., Miller, I., and Anderson, P. (1999). RNA-binding proteins TIA-1 and TIAR link the phosphorylation of eIF-2 alpha to the assembly of mammalian stress granules. J. Cell Biol. *147*, 1431–1442.

81. Anderson, P., and Kedersha, N. (2008). Stress granules: the Tao of RNA triage. Trends Biochem. Sci. *33*, 141–150.

82. Unsworth, H., Raguz, S., Edwards, H.J., Higgins, C.F., and Yagüe, E. (2010). mRNA escape from stress granule sequestration is dictated by localization to the endoplasmic reticulum. FASEB J *24*, 3370–3380.

83. Lewis, S.M., Cerquozzi, S., Graber, T.E., Ungureanu, N.H., Andrews, M., and Holcik, M. (2008). The eIF4G homolog DAP5/p97 supports the translation of select mRNAs during endoplasmic reticulum stress. Nucleic Acids Res. *36*, 168–178.

84. Jayabalan, A.K., Sanchez, A., Park, R.Y., Yoon, S.P., Kang, G.Y., Baek, J.H., Anderson, P., Kee, Y., and Ohn, T. (2016). NEDDylation promotes stress granule assembly. Nat. Commun. *7*, 12125.

85. Vattem, K.M., and Wek, R.C. (2004). Reinitiation involving upstream ORFs regulates ATF4 mRNA translation in mammalian cells. Proc. Natl. Acad. Sci. USA *101*, 11269–11274.

86. Andreev, D.E., O'Connor, P.B.F., Fahey, C., Kenny, E.M., Terenin, I.M., Dmitriev, S.E., Cormican, P., Morris, D.W., Shatsky, I.N., and Baranov, P.V. (2015). Translation of 5' leaders is pervasive in genes resistant to eIF2 repression. Elife *4*, e03971.

87. Brown, A., Baird, M.R., Yip, M.C., Murray, J., and Shao, S. (2018). Structures of translationally inactive mammalian ribosomes. Elife *7*, e40486.

88. Ligon, M.M., Joshi, C.S., Fashemi, B.E., Salazar, A.M., and Mysorekar, I.U. (2023). Effects of aging on urinary tract epithelial homeostasis and immunity. Dev. Biol. *493*, 29–39.

89. Mulvey, M.A., Schilling, J.D., Martinez, J.J., and Hultgren, S.J. (2000). Bad bugs and beleaguered bladders: interplay between uropathogenic Escherichia coli and innate host defenses *97*, 8829–8835.

90. Speich, J.E., Tarcan, T., Hashitani, H., Vahabi, B., McCloskey, K.D., Andersson, K.E., Wein, A.J., and Birder, L.A. (2020). Are oxidative stress and ischemia significant causes of bladder damage leading to lower urinary tract dysfunction? Report from the ICI-RS 2019. Neurourol. Urodyn. *39*, S16–S22.

91. Birder, L.A., Wolf-Johnston, A.S., Zabbarova, I., Ikeda, Y., Robertson, A.M., Cardozo, R., Azari, F., Kanai, A.J., Kuchel, G.A., and Jackson, E.K. (2024). Hypoxanthine Induces Signs of Bladder Aging with Voiding dysfunction and Lower Urinary Tract Remodeling. J. Gerontol. A Biol. Sci. Med. Sci. *79*, glad171. https://doi.org/10.1093/gerona/glad171.

92. Truschel, S.T., Clayton, D.R., Beckel, J.M., Yabes, J.G., Yao, Y., Wolf-Johnston, A., Birder, L.A., and Apodaca, G. (2018). Age-related endolysosome dysfunction in the rat urothelium. PLoS One *13*, e0198817.

93. Micheli, L., Leonardi, L., Conti, F., Buanne, P., Canu, N., Caruso, M., and Tirone, F. (2005). PC4 coactivates MyoD by relieving the histone deacetylase 4-mediated inhibition of myocyte enhancer factor 2C. Mol. Cell Biol. *25*, 2242–2259.

94. Vietor, I., Vadivelu, S.K., Wick, N., Hoffman, R., Cotten, M., Seiser, C., Fialka, I., Wunderlich, W., Haase, A., Korinkova, G., et al. (2002). TIS7 interacts with the mammalian SIN3 histone deacetylase complex in epithelial cells. EMBO J. *21*, 4621–4631.

95. Vietor, I., Kurzbauer, R., Brosch, G., and Huber, L.A. (2005). TIS7 regulation of the beta-catenin/Tcf-4 target gene osteopontin (OPN) is histone deacetylase-dependent. J. Biol. Chem. *280*, 39795–39801.

96. Balci, M.G., and Tayfur, M. (2018). Loss of E-cadherin expression in recurrent non-invasive urothelial carcinoma of the bladder. Int. J. Clin. Exp. Pathol. *11*, 4163–4168.

97. Zhou, Y., Liu, X., Li, W., Sun, X., and Xie, Z. (2018). Endoplasmic reticulum stress contributes to the pathogenesis of stress urinary incontinence in postmenopausal women. J. Int. Med. Res. *46*, 5269–5277.

98. Alperin, M., Abramowitch, S., Alarab, M., Bortolini, M., Brown, B., Burnett, L.A., Connell, K.A., Damaser, M.S., de Vita, R., Gargett, C.E., et al. (2022). Foundational Science and Mechanistic Insights for a Shared Disease Model: An Expert Consensus. Female Pelvic Med. Reconstr. Surg. *28*, 347–350.

99. Nesvizhskii, A.I., Keller, A., Kolker, E., and Aebersold, R. (2003). A statistical model for identifying proteins by tandem mass spectrometry. Anal. Chem. *75*, 4646–4658.

100. Dobin, A., Davis, C.A., Schlesinger, F., Drenkow, J., Zaleski, C., Jha, S., Batut, P., Chaisson, M., and Gingeras, T.R. (2013). STAR: ultrafast universal RNA-seq aligner. Bioinformatics *29*, 15–21.

101. Liao, Y., Smyth, G.K., and Shi, W. (2013). The Subread aligner: fast, accurate and scalable read mapping by seed-and-vote. Nucleic Acids Res. *41*, e108.

102. Patro, R., Mount, S.M., and Kingsford, C. (2014). Sailfish enables alignment-free isoform quantification from RNA-seq reads using lightweight algorithms. Nat. Biotechnol. *32*, 462–464.

103. Wang, L., Wang, S., and Li, W. (2012). RSeQC: quality control of RNA-seq experiments. Bioinformatics *28*, 2184–2185.

104. Robinson, M.D., McCarthy, D.J., and Smyth, G.K. (2010). edgeR: a Bioconductor package for differential expression analysis of digital gene expression data. Bioinformatics *26*, 139–140.

105. Ritchie, M.E., Phipson, B., Wu, D., Hu, Y., Law, C.W., Shi, W., and Smyth, G.K. (2015). limma powers differential expression analyses for RNA-sequencing and microarray studies. Nucleic Acids Res. *43*, e47.

106. Ritchie, M.E., Diyagama, D., Neilson, J., van Laar, R., Dobrovic, A., Holloway, A., and Smyth, G.K. (2006). Empirical array quality weights in the analysis of microarray data. BMC Bioinf. *7*, 261.

107. Liu, R., Holik, A.Z., Su, S., Jansz, N., Chen, K., Leong, H.S., Blewitt, M.E., Asselin-Labat, M.L., Smyth, G.K., and Ritchie, M.E. (2015). Why weight? Modelling sample and observational level variability improves power in RNA-seq analyses. Nucleic Acids Res. *43*, e97.

108. Law, C.W., Chen, Y., Shi, W., and Smyth, G.K. (2014). voom: precision weights unlock linear model analysis tools for RNA-seq read counts. Genome Biol. *15*, R29.

109. Schneider, C.A., Rasband, W.S., and Eliceiri, K.W. (2012). NIH Image to ImageJ: 25 years of image analysis. Nat. Methods *9*, 671–675.

110. Ligon, M.M., Wang, C., DeJong, E.N., Schulz, C., Bowdish, D.M.E., and Mysorekar, I.U. (2020). Single cell and tissue-transcriptomic analysis of murine bladders reveals age- and TNFα-dependent but microbiota-independent tertiary lymphoid tissue formation. Mucosal Immunol. *13*, 908–918.

111. Moro, C., and Phelps, C. (2023). Urothelium removal does not impact mucosal activity in response to muscarinic or adrenergic receptor stimulation. Tissue Barriers *11*, 2099214.

112. Munoz, A., Gangitano, D.A., Smith, C.P., Boone, T.B., and Somogyi, G.T. (2010). Removal of urothelium affects bladder contractility and release of ATP but not release of NO in rat urinary bladder. BMC Urol. *10*, 1–7.

KEY RESOURCES TABLE

REAGENT or RESOURCE	SOURCE	IDENTIFIER
Antibodies		
Anti-IFRD1	Abcam	Cat# ab229720; RRID:AB_3083573
Anti- Uroplakin III	Fitzgerald	Cat# 10R-U103a; RRID:AB_1289312
Anti-Puromycin	Millipore	Cat# MABE343; RRID:AB_2566826
Anti-BiP	Cell Signaling Technology	Cat# 3177; RRID:AB_2119845
Anti-ATF6	Thermo Fisher Scientific	Cat# PA5-20216; RRID:AB_11156398
Anti-XBP-1s	Cell Signaling Technology	Cat# 40435; RRID:AB_2891025
Anti-EDEM1	Proteintech	Cat# 26226-1-AP; RRID:AB_2880433
Anti-PERK	Cell Signaling Technology	Cat# 5683; RRID:AB_10841299
Anti-p-PERK	Thermo Fisher Scientific	Cat# PA5-102853; RRID:AB_2815938
Anti-eIF2α	Cell Signaling Technology	Cat# 9722; RRID:AB_2230924
Anti-p-eIF2α	Cell Signaling Technology	Cat# 3398; RRID:AB_2096481
Anti-ATF4	Abcam	Cat# ab1371; RRID:AB_300588
Anti-CHOP	Cell Signaling Technology	Cat# 2895; RRID:AB_2089254
Anti-Ki67	Abcam	Cat# ab833; RRID:AB_306483
Anti-E-Cadherin	BD Biosciences	Cat# 610181; RRID:AB_397580
Anti-p27kip1	Abcam	Cat# ab190851; RRID:AB_3083574
Chemicals, peptides, and recombinant proteins		
LongAmp® *Taq* DNA Polymerase	New England Biolabs	Cat# M0323L
DMSO	Sigma-Aldrich	Cat# D8418
Pierce IP Lysis Buffer	Thermo Fisher Scientific	Cat# 87787
Histoclear	Electron Microscopy Sciences	Cat# 64110
Hematoxylin	Fisher Scientific	Cat# 22-220-109
Eosin	Fisher Scientific	Cat# 22-050-197
FITC-dextran, 10000MW	Invitrogen	Cat# D1820
Dihydro-ethidium	Thermo Fisher Scientific	Cat# D11347
Dynabeads™ Protein A	Thermo Fisher Scientific	Cat# 10001D
X-gal	americanBIO	Cat# AB15080
Glutaraldehyde	Polysciences, Inc.	Cat# 01909
Paraformaldehyde	Thermo Fisher Scientific	Cat# 047340-9L
Critical commercial assays		
Papanicolau EA staining kit	Thermo Fisher Scientific	Cat# 22-050-211
In Situ Cell Death Detection Kit (TUNEL)	Roche	Cat# 11684795910
Deposited data		
Raw and analyzed data	Gene expression omnibus	GSE149571
Proteomics analysis	ProteomeXchange Consortium	PXD052536
Experimental models: Cell lines		
5637	ATCC	HTB9; RRID:CVCL_0126
Experimental models: Organisms/strains		
Mouse: C57BL/6	Washington University School of Medicine	Wild type
Mouse: C57BL/6	Baylor College of Medicine	Wild type
Mouse: *Ifrd1*^{tm1Lah}	Generated by Dr. Lukas Huber Medical University of Innsbruck	RRID: MGI:3043558
Oligonucleotides		
Primers used for RT-qPCR, see Table S1	This paper	N/A

Continued

REAGENT or RESOURCE	SOURCE	IDENTIFIER
Software and algorithms		
Prism v.9.0.1	GraphPad Software	http://www.graphpad.com/; RRID:SCR_002798
ImageJ v.1.54f	Wayne Rasband and contributors. NIH, USA.	https://imagej.net/; RRID:SCR_003070
Biorender licensed to Mills Lab.	Biorender	http://biorender.com; RRID:SCR_018361
Image Lab 6.1	Bio-Rad	https://www.bio-rad.com/en-us/product/image-lab-software?ID=KRE6P5E8Z; RRID:SCR_014210
AMT Image Capture Engine V602 software	Advanced Microscopy Techniques, Woburn, MA	https://amtimaging.com/home; RRID:SCR_014333
Mascot (version 2.5.1)	Matrix Science Inc Boston, MA, USA	https://www.matrixscience.com/mascot_support_v2_5.html; RRID:SCR_014322
Scaffold_4.11.0 Proteome Software	Proteome Software, Inc Portland, OR, USA	https://www.proteomesoftware.com/; RRID:SCR_014345
Protein Prophet algorithm	Nesvizhskii et al.[99]	https://proteinprophet.sourceforge.net/prot-software.html
STAR version 2.0.4b	Dobin et al.[100]	https://doi.org/10.1093/bioinformatics/bts635; RRID:SCR_004463
Subread:feature Count version 1.4.5	Liao et al.[101]	https://doi.org/10.1093/nar/gkt214; RRID:SCR_009803
Sailfish version 0.6.3	Patro et al.[102]	https://doi.org/10.1038/nbt.2862; RRID:SCR_024326
RSeQC version 2.3	Wang et al.[103]	https://rseqc.sourceforge.net/; RRID:SCR_005275
R/Bioconductor package EdgeR	Robinson et al.[104]	https://doi.org/10.1093/bioinformatics/btp616; RRID:SCR_006442
R/Bioconductor package Limma	Ritchie et al.[105]	https://doi.org/10.1093/nar/gkv007; RRID:SCR_010943
voomWithQualityWeights in Limma (version 3.28.14)	Ritchie et al.[106] Liu et al.[107] Law et al.[108]	https://www.rdocumentation.org/packages/limma/versions/3.28.14/topics/voomWithQualityWeights; RRID:SCR_010943

EXPERIMENTAL MODEL AND STUDY PARTICIPANT DETAILS

Mice

C57Bl6/J mice (8-16 weeks: WT) were obtained from the mouse facility at Washington University School of Medicine or Baylor College of Medicine. Standard rodent chow and water were available *ad libitum* throughout the experiment. *Ifrd1*$^{-/-}$ mice were a kind gift from Dr. Lukas Huber (Medical University Innsbruck) and Dr. Deborah Rubin (Washington University School of Medicine). Mice were housed in groups of four to five in a temperature- ($22 \pm 1°C$) and humidity-controlled vivarium with lights maintained on a 12:12 light/dark cycle. All animal experimental procedures were approved by the Institutional Animal Care and Use Committee at Washington University School of Medicine (Animal Welfare Assurance #A-3381-01) and Baylor College of Medicine (Animal protocol number AN-8629). All mice were humanely euthanized at the end of each experiment. Both male and female age-matched mice were used for the experiments.

Mouse genotyping

Mice were bred *Ifrd1*$^{+/-}$ to *Ifrd1*$^{+/-}$ for the generation of *Ifrd1*$^{-/-}$ mice and WT littermate controls. Each mouse used was genotyped by PCR amplification. The genomic DNA was extracted from ear tissue that was subsequently amplified using specific WT and mutant primer pairs for two different reactions (see Table S1) using Long Amp *Taq* DNA Polymerase in the presence of 5% DMSO. PCR was performed under the following settings: 94°C (Initial denaturation), 30 seconds, start cycle- 94°C, 30 seconds (Denaturation); 50°C, 30 seconds (Annealing); 65°C, 90 seconds (Extension) for 30 cycles, 65°C, 10 minutes (Final extension). The PCR products were run on 1.5% agarose gel to determine the genotype based on the presence and absence of bands in each reaction as follows: WT mouse

gives a band of 1233bp exclusively in the WT primer pair reaction and a knockout mouse gives a band of 867bp exclusively in the mutant primer pair reaction. A heterozygous mouse gives a band in both the reactions: 1233bp in WT and 867bp in mutant.

METHOD DETAILS

Cell lines

Human urinary urothelial carcinoma cell line (5637, HTB9) (ATCC) was cultured in RPMI 1640 media with 10% fetal bovine serum in a humidified atmosphere at 37°C with 5% CO2.

Immunofluorescence

Prior to sacrifice, the mouse bladders were voided, and the harvested bladders were removed and fixed in methacarn (60% methanol, 30% chloroform, and 10% acetic acid) for 20 minutes, before embedding within paraffin. The sections were deparaffinized by soaking in 3 separate solutions of 100% Histoclear for 5 minutes each. Sections were rehydrated in decreasing concentrations of ethanol (100%, 90%, 70%, 50%) for 5 minutes per concentration and soaked in 1X PBS for 5 minutes. Heat induced epitope retrieval was then performed for 5 min in sodium citrate buffer, pH 6, by subjecting the samples to high pressure in an Instant Pot. After the pressure was released, sections were washed in 1X PBS three times, for 5 minutes. Subsequently the sections were blocked in 1% bovine serum albumin for 1 hour at room temperature, followed by antibody staining with antibodies against: Uroplakin III (Fitzgerald, NA), BiP (Cell Signaling Technology, C50B12), p27kip1 (Abcam, ab190851), E-Cadherin (BD Biosciences 610181) and Ki67 (Abcam, ab833) in blocking buffer containing 0.1% Tween-20 overnight at 4°C. Sections were rinsed in 1X PBS (3 times, 5 minutes each), and incubated in appropriate fluorescently labeled secondary antibodies for 1 hour at room temperature and rinsed in 1X PBS (3 times, 5 minutes each). Sections were applied with Prolong Gold Antifade reagent with DAPI (P36935, Thermo Fisher Scientific, USA) and sealed with cover glass before proceeding with imaging. Images were taken on either a Zeiss Apotome microscope at 40x magnification or ECLIPSE Ni Epi-fluorescence Upright Microscope (Nikon, USA).

X-gal staining

For the X-gal staining on frozen bladder (WT and *Ifrd1*$^{-/-}$ mice) sections, the protocol from The Jackson Laboratory was followed. Briefly, Optimal Cutting Temperature (OCT)-frozen ten-micron bladder sections on slides were fixed in slide fixative (0.2% Gluteral-dehyde in PBS) for 10 minutes on ice. The sections were rinsed and washed in PBS for 10 minutes, and washed in detergent rinse (0.02% Igepal, 0.01% Sodium Deoxycholate, and 2mM MgCl2 in PBS) for 10 minutes. The slides were then immersed in 1 mg/ml X-gal (americanBIO; AB15080) staining solution (0.02% Igepal, 0.01% Sodium Deoxycholate, 5 mM Potassium Ferricyanide, 5mM Potassium Ferrocyanide, and 2 mM MgCl$_2$ in PBS) for 3 hours at 37°C in the dark. The slides were then post-fixed in 4% paraformaldehyde (PFA) for 10 minutes followed by a rinse and a wash in PBS, two washes in distilled water (5 minutes each), counter-stained with Nuclear Fast Red (Sigma, N8002) and rinsed in distilled water before a final wash in distilled water. Sections were then dehydrated and mounted with permount and sealed with coverslip before proceeding with imaging. For the whole organs' staining, the *Ifrd1*$^{-/-}$ mice organs (bladder, pancreas, stomach, kidney) were dissected, washed in ice-cold PBS and fixed for 2 hours in a 2% PFA/0.2% glutaraldehyde/PBS solution at 4°C. Samples were then washed three times for 10 minutes with rinse buffer (2 mM MgCl2, 0.1% Igepal in PBS) and stained for 16 hours in 1mg/ml X-gal staining solution (5 mM Potassium Ferricyanide, 5 mM Potassium Ferricyanide in rinse buffer). Subsequently, samples were washed, fixed with 4% paraformaldehyde for 16 hours, embedded in paraffin, sectioned (at 4 μm), and counter-stained with Nuclear Fast Red.

In vivo permeability assay

WT and *Ifrd1*$^{-/-}$ mice were subjected to sleep-like state using low-dose isoflurane and transferred to a holding pan to spread the limbs and expose the urethral orifice. Urine was extracted by gently pressing the abdomen. 50 μl of 10 mg/ml of fluorescein isothiocyanate (FITC)-conjugated-dextran (FITC-dextran, 10000MW, Cat. No. D1820, Invitrogen) in 1X PBS was injected transureth-rally into the bladder lumen. Mice were allowed to recover and sacrificed 1.5 hours before bladders were collected. Bladders were embedded in OCT for cryosectioning at 10 μm thickness and mounted on microscope slides. Slides were dipped in 1X PBS 5 times to remove excess OCT and added with DAPI-containing ProLong Gold antifade reagent. Sections were examined under a fluorescence microscope. Images were analyzed for FITC-dextran signal by random selection of Region of Interest (ROI) along the urothelium. Multiple ROIs from the same mouse were averaged and the mean of means were plotted to compare the fluorescent signal between the two groups. Fluorescent signals were determined by NIS Elements AR v.5.42.02 (Build 1802, Nikon, Tokyo, Japan) were used for comparison.

H&E staining

Bladder sections from WT and *Ifrd1*$^{-/-}$ mice were deparaffinized by soaking in 3 separate solutions of 100% Histoclear for 5 minutes each. Sections were rehydrated in decreasing concentrations of ethanol (100%, 90%, 70%, 50%) for 5 minutes per concentration. Staining of the nuclei was performed by soaking the sections in Hematoxylin solution for 5 minutes followed by rinsing in running tap water to remove excess Hematoxylin solution. Sections were dipped quickly into an acid alcohol solution, soaked for 5 minutes in sodium bicarbonate solution, followed by rinsing in distilled water. Staining of the cytosol was done immediately by dipping the slides

3 times in Eosin solution, soaking in increasing concentrations of ethanol (50%, 70%, 90%, 100%) for 3 minutes each, followed by a final dip in Histoclear. Sections were applied with xylene-based mounting medium, covered with cover glass, and edges were sealed with clear nail polish. Image capture was performed with a Panoramic Midi microscope (3DHISTECH Ltd, Hungary).

Transmission electron microscopy (TEM) and quantification of cell structures

Whole bladders of WT and *Ifrd1*$^{-/-}$ mice were fixed with fixative containing 2.5% glutaraldehyde and 2% paraformaldehyde in 0.1M sodium cacodylate. Samples were rinsed three times in sodium cacodylate buffer and post-fixed in 1% osmium tetroxide (Polysciences Inc.) for 1 hour, stained in 1% aqueous uranyl acetate (Ted Pella Inc., Redding, CA) for 1 hour, rinsed and dehydrated in a graded series of ethanol and embedded in Eponate 12 resin (Ted Pella Inc.). Sections of 95 nm were cut with a Leica Ultracut UCT ultramicrotome (Leica Microsystems Inc., Bannockburn, IL), stained with uranyl acetate and lead citrate, and viewed on a JEOL 1200 EX transmission electron microscope (JEOL USA Inc., Peabody, MA) equipped with an AMT 8 megapixel digital camera and AMT Image Capture Engine V602 software (Advanced Microscopy Techniques, Woburn, MA). For quantification of endolysosomes, images of superficial cells were taken at 2500x. A total of 40-97 images between the two groups (WT and *Ifrd1*$^{-/-}$) were counted to determine the number of endolysosomes per 100 μm^2 surface area examined.

TUNEL and SunSET assays

Prior to sacrifice, the mouse bladders were voided, and the harvested bladders were flash frozen using OCT. Seven-micron sections were then stained with TUNEL according to manufacturer's protocol (Roche 11684795910, *In Situ* Cell Death Detection Kit). Images were taken on a Zeiss Apotome microscope (n=3 mice). For measurement of protein synthesis via SunSET assay, the sections were fixed in 10% formalin for 15 minutes at room temperature, rinsed in 1X PBS (3 times, 5 minutes each) and then blocked in 1% bovine serum albumin containing 0.1% Triton X-100. Sections were then incubated overnight with antibody against puromycin (MABE343, EMD Millipore) at 4°C. Sections were rinsed in 1X PBS (3 times, 5 minutes each), and incubated in fluorescently labeled secondary antibody for 1 hour at room temperature and rinsed in 1X PBS (3 times, 5 minutes each). Sections were applied with Prolong Gold Antifade reagent with DAPI and sealed with cover glass before proceeding with imaging. Images were taken on ECLIPSE Ni Epi-fluorescence Upright Microscope (Nikon, USA). For quantification of puromycin signal, mean intensity of multiple ROIs from experimental replicates of a single mouse were averaged to plot the difference in intensities between the two groups (n=3 mice/group).

Urine cytology

WT and *Ifrd1*$^{-/-}$ mouse urine samples were collected for sediment analysis (10 µl urine plus 40 µl 1X PBS) and subjected to cytospin3. Sediments on the microscope slides were fixed in acetic acid/alcohol for 15 minutes and subjected to Epredia™ Papanicolaou EA Staining (22-050-211, Thermo Fisher Scientific, USA) following the manufacturer's protocol. Bright field images from a whole slide scanner were used to identify and count the sloughed urothelial cells.

In vivo ROS assay and imaging

OCT-embedded fresh young and aged bladders were cut into 10 µm thickness and mounted in glass slides for staining. Sections were soaked in ROS-sensing dye (Dihydro-Ethidium: DHE), incubated for 10 minutes at room temperature, washed in 1X PBS, and followed by counterstaining with DAPI. Fluorescent signals were determined by NIS Elements AR v.5.42.02 (Build 1802, Nikon, Tokyo, Japan) were used for comparison. Signal intensity along the urothelium of multiple images per mouse were calculated, averaged, and plotted to compare the fold-change between WT and *Ifrd1*$^{-/-}$ groups.

Void spot assay (VSA)

VSA was conducted by following protocols from previously published articles with modifications.[55–57] Briefly, individual mice (n=4/group) were placed in enclosures, lined with filter paper (Whatman #1). After a fixed interval of 4 hours, where water was withheld but food was not, the filter paper was removed, and urine spots were visualized using ninhydrin. The dried filter paper was then scanned and the number, size, and distribution of spots were quantified using Image J.[109] Each spot on the filter paper represents an individual void, with each mouse voiding a number of times throughout the 4-hour assay period. The size and area of each void was quantified.

Co-immunoprecipitation and proteomic analysis

Dynabeads Protein A for Immunoprecipitation (Thermo Fisher, 10001D) were resuspended in PBS for 10 minutes prior to incubation with anti-IFRD1 (Abcam, ab229720) and Rabbit IgG (Cell Signaling, 2729S) antibodies. For immunoprecipitation, cultured 5637 human bladder cancer cells were lysed in Pierce IP Lysis Buffer (ThermoFisher, 87787) containing Protease Inhibitor (Pierce, A32969), and incubated for 30 minutes at room temperature. The lysate was centrifuged, and supernatant transferred to the prepared Dynabeads. Beads were incubated overnight at 4°C and washed three times in PBS by gently pipetting up and down with wash buffer to remove unbound proteins. Beads were resuspended in PBS and submitted to the Proteomics Core Laboratory at Washington University in St Louis for MS/MS analysis.

    For database searching, the tandem mass spectra were extracted by the search engine Mascot (version 2.5.1). Mascot searched the UNI-HUMAN-REF-20190731 database containing 20667 entries. Mascot was searched with a fragment ion mass tolerance of

0.05.0 Da and a parent ion tolerance of 25 parts per million. In Mascot, Carbamidomethyl of cysteine was specified as a fixed modification; and the following were specified as variable modifications: Gln->pyro-Glu of the N-terminus, deamidation of asparagine and glutamine, oxidation of methionine and acetylation of the N-terminus.

Criteria for protein identification was done using Scaffold_4.11.0 Proteome Software, which validated MS/MS based peptide and protein identifications. Identification of peptides required FDR <1.0% using the Scaffold Local FDR algorithm. Proteins were identified and accepted if established at FDR <0.05% probability, with a minimum of 1 identified peptide. Proteins probabilities were assigned using the Protein Prophet algorithm[99] (Adapted from Scaffold_4.11.0).

RNA-sequencing

Preparation of bladders for RNA isolation and sequencing were done as described in Ligon et al. (2020)[110] (GSE149571). Briefly, bladders were snap frozen, homogenized and RNA isolated using RNeasy Mini Kit (Qiagen, 74101). Preparation of libraries was performed using Ribo-Zero rRNA depletion kit (Illumina) and then sequenced on HiSeq3000 (Illumina). Reads were aligned to the Ensembl GRCm38.76 top-level assembly with STAR version 2.0.4b.[100] Gene counts were produced from the uniquely aligned unambiguous reads by Subread:feature Count version 1.4.5,[101] and transcript counts were derived by Sailfish version 0.6.3.[102] Using RSeQC version 2.3,[103] sequencing performance was determined for the total number of aligned reads, total number of uniquely aligned reads, genes and transcripts detected, ribosomal fraction, known junction saturation and read distribution over known gene models. Gene counts were then imported into R/Bioconductor package EdgeR[104] and TMM normalization size factors were calculated to adjust samples for differences in library size. Ribosomal features and features not expressed in at least three samples were excluded from further analysis. TMM size factors were recalculated to create effective TMM size factors. These effective TMM factors and matrix counts were then imported into R/Bioconductor package Limma,[105] and voomWithQualityWeights[106–108] function was used to calculate the observed mean-variance relationship of every gene/transcript and sample. Gene/transcript level differential expression was evaluated using generalized linear models, which were filtered for False Discovery Rate (FDR)-adjusted p-values less than or equal to 0.05.

Real-time quantitative PCR (RT-qPCR)

Bladders of young WT and $Ifrd1^{-/-}$ mice were collected and homogenized in TRIzol™ Reagent (15596026, Thermo Fisher Scientific, USA) to extract total RNA followed by DNase I treatment (18068-015, Thermo Fisher Scientific, USA) following manufacturer's protocol. One microgram of total RNA was utilized to perform cDNA synthesis using SuperScript™ II Reverse Transcriptase (18064-014, Thermo Fisher Scientific, USA) following manufacturer's protocol. All cDNAs were diluted to 1:8 with RNase-free water prior to use. Primer designs (see Table S1) and qRT-PCR setup was performed using SsoAdvanced Universal SYBR® Green Supermix (1725274, Bio-Rad, USA) following manufacturer's protocol in 10 μl reactions (5 μl Supermix; 1 μL each of Forward and Reverse Primers; 2 μL diluted cDNA; 1 μL RNase-free water), each reaction was done in triplicate. 18S rRNA was used as a housekeeping gene. The RT-qPCR reaction was run in QuantStudio™3 Real-Time PCR System (Applied Biosystems™, USA) using the following settings: 98°C, 3 minutes (initial activation); 98°C, 30 seconds (Denaturation); 58°C, 30 seconds (Annealing/Extension); 40 cycles. Relative expression was calculated using the Double Delta Ct Value and normalized to 18S.

Stripped bladder epithelium

WT and $Ifrd1^{-/-}$ mice were euthanized and bladders were extracted and placed on petri dish with ice-cold 1X PBS, divided into 3 longitudinally cut sections, and dissected to separate lamina propria from the detrusor muscle. Isolated lamina propria were then scraped gently with scalpel blade to collect the urothelium layer [111,112]. Liquid suspension of urothelial cells was transferred into a clean 5 mL cone-bottom tube and spun quickly for 10 seconds at 300 rpm. Supernatant was discarded and pellet was resuspended in RIPA lysis buffer supplemented with Protease and Phosphatase inhibitors for total protein extraction and western blotting.

Western blotting

WT and $Ifrd1^{-/-}$ bladders of young mice were collected and homogenized in RIPA lysis buffer to extract total proteins. Total protein was quantitated using a BCA assay (Pierce™ BCA Protein Assay Kit, 23225, Thermo Fisher Scientific, USA). 10-30 μg of protein was loaded onto precast gel (NP0321, NuPAGE™ 4-12%, Bis-Tris, Mini Protein Gels, ThermoFisher Scientific, USA) and resolved at 135 volts for 90 minutes. Protein bands were immobilized through transfer to PVDF membrane (IPFL00010, Immobilon Transfer Membrane, Millipore, Ireland) for 90 minutes at 30 volts in ice using the NuPAGE™ Transfer Buffer (20X) diluted to 1X in the presence of 10% Methanol. The membrane was treated with blocking buffer (927-60001, Intercept® [TBS] Blocking Buffer, LI-COR, USA) for 1 hour at room temperature with gentle agitation. Membranes were incubated with primary antibody [IFRD1 (abcam, ab229720), BiP (CST, 3177S), ATF6 (Thermo Fisher, PA5-20216), XBP1 (CST, 40435S), EDEM1 (Proteintech, 26226-1-AP), PERK (CST, 5683S), p-PERK (Thermo Fisher, PA5-102853), eIF2α (CST, 9722S), p-eIF2α (CST, 3398S), ATF4 (Abcam, AB1371), CHOP (CST, 2895S)] solution (1:1000) in blocking buffer plus 0.1% Tween-20, overnight at 4°C with agitation. Beta-actin (CST, 3700S) was used as a loading control. Membranes were washed in 1X TBS with 0.1% Tween-20, 5 times, for 5 minutes each at room temperature with agitation followed by treatment with appropriate secondary antibody solution in blocking buffer plus 0.1% Tween-20 for 1 hour at room temperature with agitation. Membranes were washed in 1X TBS with 0.1% Tween-20, 5 times, for 5 minutes each at

room temperature with agitation followed by washing in 1X TBS 2 times, for 5 minutes each. Imaging was performed using the ChemiDoc™ MP imaging system (Bio-Rad, USA). Densitometric analysis was done using Bio-Rad Image Lab software (6.1).

QUANTIFICATION AND STATISTICAL ANALYSIS

All measured values were plotted using GraphPad Prism versions 9.0.1 to 10.2.2 (GraphPad Software, La Jolla, CA, USA). Standard statistical approaches were used. For data that would obviously not be normally distributed based on experimental design or data that exhibited highly non-equal variance or obvious non-normalcy, a non-parametric rank-sum test was used (Mann-Whitney for Figures 2E, 2G, 3D, 3F, 3G, 4C–4G, 4I, 4J, 4L–4N, 4P–4T, 4V–4W, and 5F), otherwise unpaired t-tests were used when data approximated normal distribution (for Figures 5B, 5C, 5I, and 5J). "n" for each experiment and statistical test used are indicated in figure legends. Data were expressed as mean ± Standard Deviation (SD, for Figures 2G, 3F, 3G, 4C–4G, 4I, 4J, 4L–4N, 4P–4T, 4V, 4W, 5B, 5C, 5F, 5G, and 5J) and where means of means were plotted, data were expressed as ± Standard Error of the Mean (SEM, for Figures 2E, 3D, and 5I).